Solid Earth
Discussions

Structural and rheological evolution of the Laramide subduction channel in southern California

Haoran Xia[1], John P. Platt[1]

5   [1]Department of Earth Sciences, University of Southern California, Los Angeles, CA 90089-0740, USA

Correspondence to: Haoran Xia (haoranxi@usc.edu)

Abstract. The Pelona schist in the San Gabriel Mountains, southern California, formed in the Laramide subduction channel, exhibits multiple phases of deformation/metamorphism and provides valuable insights into the rheological properties of the subduction channel. Petrological and microstructural analysis indicates that the Pelona schist has undergone three major

10   deformational/metamorphic events. Subduction of volcanic and sedimentary protoliths during D1 was recorded by aligned mineral inclusions in albite and epidote porphyroblasts. Metamorphic temperature and pressure at the end of subduction yielded by Raman spectroscopy of carbonaceous material and Si-in-muscovite barometry were 518.9 ± 19.6 °C and 10.5 ± 0.4 kbar, respectively. During D1 the dominant deformation mechanism was quartz pressure solution, and the estimated shear stress and strain rate were less than 10 MPa and 5.8×10^{-13} s^{-1}. D2, the first stage exhumation of the Pelona schist along

15   the upper section of the subduction channel during return flow, was recorded by retrogressive metamorphism, isoclinal folding, and a pervasive schistosity that wraps around earlier porphyroblasts. Metagreywacke was deformed mainly by quartz pressure solution and metachert was deformed dominantly by dislocation creep during D2. The shear stress in metagreywacke was less than 10 MPa and that in metachert was between 8.6 and 13.3 MPa, resulting in a strain rate of 1.4×10^{-13} to 5.5×10^{-13} s^{-1}. A topography driven model is proposed as the main driving force of D2 exhumation. D3 records

20   normal-sense movement on the Vincent fault, which separates the schist from overlying arc and continental basement. This resulted in the second stage of exhumation, creating a major synform and associated mylonitic fabric in the upper section of the Pelona schist. Conditions at the beginning of D3 were 390°C and 5.8 kbar given by the TitaniQ thermometer and phengite barometer. The deformation was dominated by quartz dislocation creep with a strain rate of ~5.1×10^{-13} s^{-1} at a shear stress of ~22 MPa.

25   1 Introduction

Subduction zones are convergent plate boundaries where one plate descends beneath the overriding plate. Along with the down-going slab, poorly consolidated sediment is dragged and deformed, forming a subduction channel between the converging plates (Cloos and Shreve, 1988; Gerya and Stockhert, 2002). Not all the sediment in the channel is subducted; part of it may be exhumed after experiencing high pressure-low temperature metamorphism. Various models have been

proposed to interpret the burial and exhumation cycle of high-pressure subduction complexes in accretionary settings (Brandon et al., 1998; Brun and Faccenna, 2008; Platt, 1993; Ring et al., 2007). The best way to test these models is to examine the deformational and metamorphic history of the exhumed rocks from a subduction channel.

5 The rheological properties of subduction channels may place controls on the interaction of the converging plates, such as depth of seismicity (e.g., Ruff and Tichelaar, 1996) and coupling of the plates (e.g., Stöckhert, 2002). Geophysical observations cannot easily yield the mechanical properties of the plate interface in active subduction zones (Grigull et al., 2012; but see Houston, 2015). The only directly available information on the small scale deformation mechanisms, stress states and material strength along the plate interface comes from the rocks exhumed from a subduction zone (e.g.,

10 Wassmann and Stöckhert, 2013).

The Pelona schist in the Transverse Ranges, southern California was formed during the Late Cretaceous-Paleocene Laramide subduction event, and it is an ideal case to scrutinize the subduction zone. In this paper we first construct the deformational and metamorphic history of Pelona schist, and then we infer deformation mechanisms and rheological properties along the

15 subduction channel.

2 Geologic background

Laramide subduction caused eastward migration of magmatic activity in western North America from Late Cretaceous to early Tertiary time; this, together with basement-involved thrusting in the Laramide foreland, led to the idea that this was a period of flat-slab subduction (Coney and Reynolds, 1977; Dickinson and Snyder, 1978). Although debates exist (e.g., Barth

20 and Schneiderman, 1996; Ehlig, 1981), it is widely accepted that the Pelona, Orocopia, and Rand schists and the schists of Portal Ridge and Sierra de Salinas in southern California and adjacent areas are products of this subduction event (e.g., Burchfiel and Davis, 1981; Crowell, 1981; Grove et al., 2003; Hamilton, 1988; Jacobson et al., 2007), and that their protolith ages decrease from northwest to southeast (Grove et al., 2003). These ocean-affiliated schists were metamorphosed under moderately high-pressure conditions from blueschist facies to amphibolite facies beneath the Cordilleran Mesozoic

25 magmatic arc, and generally preserve retrograde metamorphic textures (e.g., Chapman et al., 2010; Jacobson, 1995a; Kidder and Ducea, 2006).

Nowadays the schists are separated from the upper plate of Precambrian to Mesozoic igneous and metamorphic rocks by normal faults. For the Rand schist and the schist of Sierra de Salinas, Chapman et al. (2010) suggested that the contact between the schists and the upper plate was remobilized as a normal fault during exhumation even though it was proximal to

30 the original subduction megathrust. In the Orocopia Mountains, Jacobson and Dawson (1995) interpreted the upper boundary of the Orocopia schist as an early Miocene low-angle detachment fault, underlain by a thin zone of mylonitized and

retrogressed schist. However, the Vincent fault above the Pelona schist, which is also known as the "Vincent thrust", was argued to be the original subduction megathrust (Ehlig, 1981; Jacobson, 1983b; Jacobson et al., 1996).

The Pelona schist occurs in the Sierra Pelona and in the eastern San Gabriel Mountains of the Transverse Ranges (Fig. 1); we
5   focus on the latter in this paper because of the outstanding exposures along the East Fork of the San Gabriel River. The Pelona schist in the East Fork area is separated by the regionally gently SW-dipping Vincent fault from a Meso-Proterozoic gneiss complex and Mesozoic granitoid rocks in the hanging wall (Fig. 2), which formed part of the Mesozoic arc in California. A mylonite zone is developed in the lower 500 to 1000 m of the hanging wall. The Pelona schist in the East Fork area occurs in the core of a NW-trending post-metamorphic antiform (Jacobson, 1997), and is truncated to the NE by the
10 Punchbowl and San Andreas faults (Dibblee, 1967). Through the approximately 4km thick transect in the East Fork, the Pelona schist consists of ~ 90% metagreywacke, ~10% greenschist and a minor amount of metachert (Jacobson, 1997), all of which were metamorphosed under high-pressure greenschist facies conditions. The peak pressure and temperature were constrained in the Sierra Pelona at up to 10 ± 1 kbar and 620-650°C (Graham and Powell, 1984). An inverted thermal gradient in the Pelona schist was reported both in the Sierra Pelona (Graham and Powell, 1984) and in the East Fork of the
15 San Gabriel Mountains (Jacobson, 1983a, 1995a). The protolith of the Pelona schist has a maximum age of 68 Ma based on detrital zircon $^{206}Pb/^{238}U$ dating (Grove et al., 2003). Hornblende $^{40}Ar/^{39}Ar$ ages from mafic schist in the East Fork are 60.3 ± 2.6 Ma and 58.9 ± 2.5 Ma (Jacobson, 1990), and muscovite $^{40}Ar/^{39}Ar$ ages cluster between 55.5 Ma and 60.8 Ma (Grove et al., 2003; Jacobson, 1990) though one metagreywacke sample from the deepest structural level yields a muscovite $^{40}Ar/^{39}Ar$ age of 31.7 ± 0.2 Ma. To improve the precision of cooling history of the Pelona schist, in this study we also performed
20 zircon fission track analyses as presented in Sect. 5.4.

A striking feature of the Pelona Schist is the complete lack of intrusive rocks related to the Late Cretaceous arc that directly overlies the Vincent fault. A phase of Miocene magmatic activity in the East Fork area, however, is characterized by intermediate dykes and sills in both the upper plate and the Pelona Schist, and a dacite sill complex with a cumulative
25 thickness of a few tens of meters parallel to the main schistosity of the Pelona Schist near Iron Fork, which was dated at 14-16 Ma by the K/Ar method (Miller and Morton, 1977).

3 Methods

3.1 Thermobarometers

3.1.1 Raman spectroscopy on carbonaceous material (RSCM)

30 Organic material in rocks undergoes irreversible graphitization during prograde metamorphism, and the degree of this transformation is a function of temperature and is not subject to retrogression, so the temperature measured by this approach

approximates the maximum temperature (Beyssac et al., 2002). The degree of organization of carbonaceous material can be measured using Raman microspectroscopy by calculating ratios of the peak areas at bands of 1350 cm^{-1}, 1580 cm^{-1}, and 1620 cm^{-1}. The calibration used here (Beyssac et al., 2002) comes with a maximum error of ± 50 °C, stemming from the uncertainties in the thermobarometric methods used to calibrate it. The precision of the method, however, is ~10°C (Beyssac

5   et al., 2002). RSCM measurements of carbon-rich metagreywacke samples were completed with a 514 nm argon laser in the Mineral Microspectroscopy Facility at the California Institute of Technology and the spectra were processed with the software Peakfit following the procedure outlined in Beyssac et al. (2002).

3.1.2 Quartz c-axis fabric opening-angle thermometer

The empirical quartz c-axis fabric opening-angle thermometer (Kruhl, 1998) utilizes the linear relationship between the

10   opening angle of quartz c-axis fabric and the temperature during fabric formation. This deformation-related thermometer has an uncertainty of ± 50 °C, and is applicable for rocks deformed in the ~300-650 °C range. Kruhl (1998) noticed that at given temperatures, the opening angles of quartz c-axis fabrics from experimentally deformed rocks at high strain rates are smaller than those from naturally deformed rocks, but he argued that strain rate should not affect the thermometer when applied to rocks deformed at natural conditions because the thermometer was established on rocks deformed at natural strain rates. By

15   promoting prism [c] slip, high water content may result in larger opening angles of fabrics, but the direct link between water content and opening angle of quartz fabric has not yet been demonstrated experimentally (Law, 2014). Quartz fabrics, or crystallographic preferred orientations (CPO), were measured and analyzed using a Hikari electron backscatter diffraction (EBSD) detector mounted on a JEOL-7001F scanning electron microscope at Center for Electron Microscopy and Microanalysis, University of Southern California and associated OIM collection/analysis software developed by EDAX. The

20   acceleration voltage was 25 kV, the working distance 15 mm, and the step size half of the pre-estimated average grain size.

3.1.3 Titanium-in-quartz thermobarometer (TitaniQ)

The substitution of Si by Ti in quartz is P and T dependent and it enables P-T estimation by measuring titanium content in quartz (Thomas et al., 2010; Wark and Watson, 2006), together with another thermobarometer. Calibrations have performed at constant pressure (Wark and Watson, 2006) and varying pressure conditions (Thomas et al., 2010) by synthesizing quartz

25   and rutile from silica-saturated aqueous fluids. The uncertainty in the temperature determined using the calibration of Thomas et al. (2010) is approximately ± 20 °C if the error of the independently constrained pressure is ± 1 kbar. Huang and Audétat (2012) determined an alternative calibration by assuming that their lowest Ti concentration measurements were closest to equilibrium. Thomas et al. (2015) evaluated the published calibrations by synthesizing and then recrystallizing quartz at different P-T conditions, and confirmed the validity of the calibration of Thomas et al. (2010), which we used in

30   this study. Samples were first examined by cathodoluminescence imaging using a Tescan Vega-3 XMU scanning electron microscope at University of California, Los Angeles, and were then measured on a Cameca IMS 6f secondary ion mass

spectrometer (SIMS) at Arizona State University. SIMS settings and analytical procedures followed those given by Behr et al. (2011).

3.1.4 Phengite geobarometer

The composition of the muscovite-celadonite solid solution series is a function of pressure and temperature. Substitution of
5 celadonite for muscovite, resulting in higher Si content, is favored by increasing pressure and decreasing temperature, based on which Massonne and Schreyer (1987) established a phengite geobarometer. The calibration is based on independent P-T estimates from coexisting mineral assemblages, and is subject to large uncertainties. Mineral analyses were performed on a JEOL JXA-8200 electron microprobe at University of California, Los Angeles. The acceleration voltage was 15 kV, the beam current 10 nA and the beam diameter 5-8 μm.

10 ## 3.2 Recrystallized grainsize piezometry for quartz

3.2.1 Grainsize measurements

Two approaches were employed to measure quartz grainsize. For samples with grainsize more than 50 μm, grain boundaries were manually traced on the optical photomicrographs and then the grainsize was measured in ImageJ. When the grainsize is less than 50 μm, EBSD was used to improve the precision. The settings for EBSD analyses are similar to those for c-axis
15 fabric measurement, except that the step size of mapping was ensured to be less than one fifth of the average grainsize.

3.2.2 Stress calculation

Differential stress was calculated using quartz recrystallized grain size piezometer $D = 10^{3.56\pm0.27} \times \sigma^{-1.26\pm0.13}$, where D is the grain size of recrystallized quartz in microns and σ is the differential stress in MPa (Stipp and Tullis, 2003). Differential stress calculated from the previous equation was multiplied by a factor of 0.73 to correct for possible errors in the stress
20 measurements on the Griggs-type apparatus used for the original calibration (Holyoke and Kronenberg, 2010). The piezometer can be applied to quartz recrystallized grain size up to 120 μm (Stipp et al., 2010). Within uncertainties, the piezometer is independent of the water content of the quartz, temperature, and the quartz alpha-beta phase transition (Stipp et al., 2006). Shear stress in a plane stress setting was calculated from differential stress by dividing by $\sqrt{3}$ (Behr and Platt, 2013).

25 ## 3.3 Detrital zircon fission track analysis

Detrital zircon fission track analysis was performed on six metagreywacke samples by Apatite to Zircon, Inc. The Pb content was measured using Agilent 7700x LA-ICP-MS mounted with Resonetics RESOlution M-50 laser ablation system.

4 Deformation structures of the Pelona schist in the eastern San Gabriel Mountains

4.1 Field occurrence

The Pelona schist in the San Gabriel Mountains consists mainly of metagreywacke (Fig. 3d) with minor amounts of mafic greenschist (Fig. 3c) and metachert (Fig. 3a), all of which were metamorphosed up to high-pressure greenschist facies. The
5 typical mineral assemblage of metagreywacke is albite + quartz + white mica + chlorite + stilpnomelane + epidote + sphene with garnet grains and graphitized carbonaceous material in the albite porphyroblasts. The composition of garnet changes from spessartine rich in the core to grossular rich in the rim (Jacobson, 1983a). Greenschist is made up of amphibole + albite + chlorite + epidote + quartz + sphene. Amphibole here is actinolite to actinolitic hornblende with high Na/Al ratio (Jacobson, 1997). Metachert consists of quartz and trace amount of stilpnomelane, albite and garnet. Calcite can be found in
10 all three rock types. Boudinaged quartz veins are common in greenschist.

The earliest fabric (S1) in the Pelona schist is preserved as straight inclusion trails in albite porphyroblasts in metagreywacke, and in albite and epidote porphyroblasts in greenschist (see Sect. 4.2, below). The dominant deformation structure in the Pelona schist is folding of the compositional layering (Fig. 3a, b, d and e). Two types of the folds have been
15 recognized in the field: 1) pervasive tight isoclinal folds (Fig. 3a, b and d) and 2) the large-scale Narrows synform and associated minor folds (Fig. 3e). Isoclinal folds occur pervasively in the East Fork transect, and are characterized by their tightly closed limbs with a length varying from less than a meter to a few tens of meters. SW-dipping axial-planar schistosity (S2) is well developed. Sheath folds (Fig. 3b) and axis-parallel stretching lineation indicate SE-NW stretching. The Narrows synform and associated minor folds occurred in the upper 700 m section of the Pelona schist, and refold the isoclinal folds.
20 The Narrows synform is more open, but its hinge is generally parallel to those of the isoclinal folds. Moderate SW-dipping axial-planar crenulation cleavage (S3) is developed in the Narrows synform. The overturned upper limb of the Narrows synform is cut by the Vincent fault. Both S2 and S3 are moderately SW dipping and the pervasive sub-horizontal stretching lineation trends SE.

4.2 Microstructures of Pelona schist in the Vincent Gulch of San Gabriel Mountains

25 #### 4.2.1 D1 fabrics

S1 is preserved by the trails of mineral inclusions in albite porphyroblasts in metagreywacke (Fig. 4a), and in epidote and albite porphyroblasts in greenschist (Fig. 4d). The mineral inclusions are white mica, epidote, quartz, garnet, zircon and abundant carbonaceous material. Some of the trails are rich in carbonaceous material or mica while others are rich in quartz, which define a differentiated cleavage. Orientation of S1 varies from one porphyroblast to another. Quartz in S1 has a
30 grainsize ranging from 10 to 50 μm and shows a random CPO (Fig. 4c). No undulose extinction or recrystallization was observed in included quartz.

4.2.2 D2 fabrics

Metagreywacke. As described above, the cores of the albite grains contain mineral inclusions. Rims of some albite porphyroblasts are free of inclusions, which probably resulted from overgrowth. Albite does not show recrystallization or

5   undulose extinction. A few albite grains were broken apart with quartz deposited in between (Fig. 5a). White mica and chlorite are strongly differentiated into P-domains and define S2 (top stripe of Fig. 5b), which wraps around the albite porphyroblasts. In the hinges of isoclinal folds, the trails of minerals included in albite (S1) were crenulated (Fig 4b), which might represent an early stage in the development of S2.

10   Quartz crystals in Q domains, and in strain shadows around albite and epidote porphyroblasts, are equant and coarse-grained (100 to 200 μm), with trails of fluid inclusions and relatively straight grain boundaries, though bulging occurs in some crystals (Fig. 5b, c and d). They show undulose extinction. Quartz crystals in P domains (mica-rich areas) have a large aspect ratio (more than 2) and a grainsize of ~30 to 100 μm (Fig. 5b and c).

15   Shear sense indicators are not common in the metagreywacke. Shear bands and asymmetric albite porphyroblasts are the only two types of shear sense indicators found in the samples deeper than the Iron Fork. They show a top-to-NW sense of shear (Fig. 5e). In the Iron Fork area, conjugate shear bands are observed and no consistent shear sense can be inferred (Fig. 5f). In the samples shallower than the Iron Fork, S2 has been overprinted by S3 and its sense of shear cannot be inferred.

20   **Metachert.** Quartz grains exhibit equant grain shape and relatively straight grain boundaries, which may be pinned by oriented white mica. Most quartz grains show weak undulose extinction and deformation lamellae occur in a few cases. In the structurally lowest level near Prairie Fork, the grainsize ranges from 100 to 300 μm and the average is 136 ± 47 μm (Fig. 6a). In samples from Fish Fork and Iron Fork that were not strongly annealed, quartz shows evidence of recrystallization by subgrain rotation and/or grain boundary migration (Fig. 6b). The average recrystallized grain size varies between 47 μm and

25   82 μm (Table 1). Quartz c-axis pole figures of samples close to Prairie Fork exhibit maxima around the z-axis and a sub-maximum near the y-axis (Fig. 6c) while samples near Iron Fork show crossed girdles (Fig. 6d).

Sense of shear in metachert can be inferred from quartz c-axis pole figures and shear bands. For rocks deeper than Iron Fork, the quartz CPO of a Prairie Fork sample exhibits a top-to-SE shear sense (Fig. 6c) and the shear bands of a Fish Fork sample

30   show a top-to-NW sense of shear (Fig. 6e). For rocks downstream from the Iron Fork, quartz new grain shape fabric and CPO's show a consistent top-to-SE sense of shear (e.g., Fig. 6b, d and f).

Greenschist. Chlorite, actinolite, tabular albite and epidote define S2 (Figs. 7a and b). As in the metagreywacke, albite in greenschist also exhibits evidence of overgrowth (Fig. 7c). Quartz is concentrated in strain shadows around epidote porphyroblasts or magnetite (Fig. 7d). Most of the quartz is recrystallized by grain boundary migration or subgrain rotation.

4.2.3 D3 fabric

5   S3 is best preserved in the metagreywacke in the hinge and upper limb of the Narrows synform; the S2 foliation was strongly crenulated, and the axial planes of the crenulation define S3 (Fig. 8a).

In the upper limb of the Narrows synform, quartz is completely recrystallized by subgrain rotation (SGR), and the recrystallized grainsize clusters around 30 μm. Noticeably, some of the grain boundaries of the recrystallized quartz grains
10   show an irregular shape due to bulging, forming fine-grained quartz crystals (Fig. 8b). Albite remains intact and does not show any evidence of plastic deformation.

The top ~100 m of the Pelona Schist immediately beneath the Vincent fault exhibits strong mylonitic microstructure. Quartz grains have been completely recrystallized by SGR, showing a new grain shape fabric and indicating a top-to-SE sense of
15   shear. The grainsize of recrystallized quartz is around 18 μm (Fig. 8c). In thin sections cut perpendicular to the lineation, axial planes of muscovite crenulations are parallel to the shape preferred orientation of recrystallized quartz (Fig. 8d). This suggests that crenulation of muscovite due to the Narrows synform was coeval with mylonitization along the Vincent fault.

4.3 Sense of shear during the deformation history

Here we summarize information on the sense of shear in the Pelona schist.
20   • It is not possible to determine the sense of shear during D1, as its original orientation was strongly modified during later deformation.
   • The sense of shear during D2 varies depending on the structural level. For rocks structurally deeper than Iron Fork, though exceptions exist, the shear bands in metagreywacke and metachert show a top-to-NW sense of shear (Figs. 5e and 6e). One exception is a metachert sample (Figs. 6a and c) that has a quartz pole figure that suggests a top-to-
25   SE sense of shear. This sample has annealed and its CPO might have been altered during annealing. For rocks shallower than Iron Fork, quartz pole figures of metachert samples show a top-to-SE sense of shear. The sense of shear in the Iron Fork area is complicated. Metachert samples from the Iron Fork and structurally above all exhibit a top-to-SE sense of shear, whereas boudinaged quartz veins in greenschist that is a few tens of meters structurally higher than Iron Fork exhibit an apparent top-to-NW sense of shear (Fig. 3c).
30   • The quartz new grain shape fabric developed during D3 implies a top-to-SE sense of shear.

Solid Earth
Discussions

Open Access

EGU

5 P-T-t path of Pelona schist

5.1 Peak metamorphic temperature

Raman spectroscopy on carbonaceous material (RSCM) and the opening angle of quartz c-axis fabric thermometer were used to quantify the peak metamorphic temperature and/or to detect any possible inverted thermal gradient. A series of

5 carbon-rich metagreywacke samples from a 4km thick transect of Pelona Schist yield an average peak temperature of 518.9 ± 19.6 °C (see Table S1 for sample locations and Table S2 for detailed analysis results). All but a couple of the measurements lie within uncertainty of ~ 512 °C, and there is no obvious systematic trend of peak temperature across the East Fork cross-section (Fig. 9). The average peak temperature of metachert given by the quartz c-axis fabric opening-angle thermometer is 547 ± 18 °C. Considering that this thermometer has an uncertainty of ± 50 °C, the peak temperature given by

10 this thermometer is consistent with that from RSCM.

5.2 Peak metamorphic pressure

Within the isoclinal folds, muscovite wrapping albite in metagreywacke exhibits straight grain shapes parallel to the axial plane (S2) and is optically strain free. The lack of large muscovite grains in albite porphyroblasts indicates that the muscovite outside albite presumably crystallized during S2 at or after peak conditions. The phengite barometer requires a

15 mineral assemblage of phengite, K-feldspar, phlogopite and quartz, whereas it will give a minimum pressure if phengite only coexists with a (Mg Fe)-silicate (Massonne and Schreyer, 1987). Samples analyzed were all metagreywacke with a mineral assemblage of phengite + quartz + stilpnomelane/biotite and do not contain K-feldspar, so the results given by this barometer are minimum pressures. The average Si content is 3.39 ± 0.03 atoms per formula unit (a.p.f.u.) of white mica, i.e, $K(Mg, Fe^{2+})_x Al_{2-x}[Si_{3+x}Al_{1-x}O_{10}](OH)_2$ where x is the number of Mg and Fe^{2+} atoms in the octahedral site (see Tables S1 and

20 S3 for sample locations and analysis results). These results are consistent with the old muscovite grain compositions reported by Jacobson (1983a, 1984). Combined with the peak temperature, the peak pressure is 10.5 ± 0.4 kbar. The result is similar to 10 ± 1 kbar, the peak pressure of Pelona schist in Sierra Pelona (Graham and Powell, 1984). The peak pressure corresponds to a depth of approximately 37 km.

5.3 P-T conditions of mylonitization of Pelona schist

25 In mylonitized metagreywacke, coarse-grained muscovite grains defining S3 are curved and show undulose extinction whilst fine-grained muscovites are usually free of strain. Some grains show compositional zonation in backscattered electron images. Electron probe results indicate that the cores of the zoned muscovite have Si content (~3.35 a.p.f.u.) similar to that of S2 muscovite, and the rims of the zoned muscovite have Si content similar to that of fine-grained muscovite (~3.25 a.p.f.u.; see Table S1 for sample locations and Table S3 for analysis results). Quartz in one metagreywacke sample collected

30 close to the Vincent fault, which has a mylonitic microstructure as described previously, reveals a titanium concentration of 1.55 ± 0.17 ppm (see Table S1 for sample location and Table S4 for analysis results). Combination of phengite barometry

and TitaniQ thermobarometry yields an average P of 5.8 ± 0.8 kbar and T of 390 ± 13 °C, which can be attributed to this stage in the structural development of the schist.

5.4 Timing of exhumation of Pelona schist

5   Several high-temperature and low temperature thermochronological studies of Pelona schist have been reported. The youngest $^{206}Pb/^{238}U$ age of the detrital zircon from the Pelona schist is 68 Ma (Grove et al., 2003), marking the earliest possible time for the subduction of the protolith of the Pelona schist. Three hornblende $^{40}Ar/^{39}Ar$ ages from the greenschist in the East Fork area reported are 58.9 ± 2.5 Ma, 60.3 ± 2.6 Ma and 73.4 ± 3.0 Ma (Jacobson, 1990). As the youngest detrital zircon $^{206}Pb/^{238}U$ age suggests that underthrusting of the Pelona schist had not started until 68 Ma, the 73.4 Ma hornblende $^{40}Ar/^{39}Ar$ age is unlikely to be reliable. The closure temperature of hornblende is about 500°C, and the hornblende $^{40}Ar/^{39}Ar$

10   age should be the cooling age because the peak metamorphic temperature of Pelona schist is above this closure temperature. Muscovite $^{40}Ar/^{39}Ar$ ages of the Pelona schist in the East Fork area cluster between 55.5 ± 0.3 Ma and 60.8 ± 0.6 Ma, though one sample from Prairie Fork yields 34.2 ± 0.2 Ma (Grove et al., 2003; Jacobson, 1990). The 55-61 Ma ages are likely to date cooling below ~400°C, and may be approximately coeval with mylonitization.

15   To better constrain the time when the Pelona schist entered the brittle regime, we performed zircon fission track analysis on six metagreywacke samples from East Fork in this study. The zircon fission track age is as old as ~46.9 Ma immediately beneath the Vincent fault, and becomes progressively younger toward the north except one outlier (~13.5 Ma) probably due to Miocene magmatic activity (see Table S1 for sample locations and Table S5 for analysis results). The sample from Prairie Fork has the youngest age of ~23.5 Ma, which confirms the $^{40}Ar/^{39}Ar$ age of ~34.2 Ma (Grove et al., 2003) from the same

20   area. The results above imply that the top section of the Pelona schist cooled through the zircon fission track closure temperature of ~230°C around ~46.9 Ma, and that the structurally deeper section of the schist experienced slow cooling over the next 20 million years.

5.5 Discussion

5.5.1 Deformation history

25   We make the case here that the main foliation (S2) of the Pelona schist in the San Gabriel Mountains preserves mineral assemblages and microstructures of retrograde metamorphism based on the following observations: 1) biotite rarely appears in the Pelona schist in the San Gabriel Mountains, whereas biotite is more common in the Pelona schist in Sierra Pelona (Graham and England, 1976; Graham and Powell, 1984); 2) garnet occurs exclusively as inclusions in albite porphyroblasts, where it was protected from retrogression; 3) the compositional zonation of muscovite indicates decompression and hence

30   exhumation during its formation. A plausible explanation for these observations is that the Pelona schist in the San Gabriel

10

Mountains experienced retrograde metamorphism during which biotite and garnet were broken down to chlorite and white mica.

If S2 was formed during exhumation, it is likely that S1 formed during subduction, while S3 is related to later reactivation and mylonitization. As discussed in Sect. 4.2.3, S3 is characterized by crenulation of S2 and mylonitization, and therefore is inferred to postdate S2. Mylonitized Pelona schist shows similar stress, pressure and temperature conditions as the low-stress mylonites right above the Vincent fault in the upper plate (Xia and Platt, in preparation), so the mylonitization of Pelona schist could have occurred contemporaneously with the low-stress mylonite in the upper plate. The overturned limb of the Narrows synform was cut by the Vincent fault, indicating that the latest activity of the Vincent fault was no earlier than S3. Considering the spatial parallelism of the mylonitic foliation and the Vincent fault, a simple explanation for the temporal relationship between D3, during which the Narrows synform and mylonitization occurred, and the latest movement along the Vincent fault could be that they took place at approximately the same time.

5.5.2 P-T-t path of Pelona schist

With the above data, we are able to establish the metamorphic and deformational history of the Pelona schist. The youngest detrital zircon ^{206}Pb/^{238}U age of ~68 Ma places constraints on the youngest age of the source rock of the Pelona schist and on the earliest time of the subduction initiation. The peak conditions are 10.5 ± 0.4 kbar and 518.9 ± 19.6 °C as indicated by the phengite barometer and RSCM. The timing of peak metamorphism is not known precisely, but it should be no later than ~60.3 Ma as constrained by the hornblende ^{40}Ar/^{39}Ar age of the greenschist in the Narrows area. After reaching these conditions, part of the Pelona schist was underplated and exhumed, firstly by ductile flow during D2, and then by normal sense motion on the Vincent Fault, accompanied by formation of the Narrows synform and associated mylonite (D3). The P-T conditions during mylonitization were 5.8 kbar and 390°C given by the phengite barometer and the TitaniQ thermometer. Mylonitization of the top section of the schist started at ~55 Ma implied by the muscovite ^{40}Ar/^{39}Ar ages and ceased by ~43 Ma as constrained by the zircon fission track ages of the schist immediately beneath the Vincent fault (Fig. 10).

5.5.3 Inverted thermal gradient of Pelona schist

Pelona schist in the Sierra Pelona was metamorphosed up to amphibolite facies and shows an upward transition from high-pressure greenschist facies to amphibolite facies. The temperature ranges from ~480°C to 620 - 650 °C upward in a ~700 m thick transect, corresponding to an inverted thermal gradient of 170 to 250 °C km^{-1} (Graham and Powell, 1984). In contrast, the Pelona schist in the East Fork was metamorphosed to high-pressure greenschist facies and its peak metamorphic temperature is lower than that in the Sierra Pelona by about 100 °C. No inverted thermal gradient can be observed in the East Fork. It is possible that no inverted thermal gradient was developed in East Fork area, though it cannot be excluded that the high temperature section of the Pelona schist in the San Gabriel Mountains was cut off by the Vincent fault.

6 Exhumation mechanisms of the Pelona schist

Various models such as upper plate normal faulting (e.g., Jacobson et al., 2007), passive-roof thrusting and erosion (Yin, 2002), return flow (Oyarzabal et al., 1997), and channelized extrusion (Chapman et al., 2010) have been proposed to explain the exhumation of the Rand schist, the schists of Portal Ridge and Sierra de Salinas, and the Orocopia schist. As for the Pelona schist, it was still thought to preserve the original structural and metamorphic features related to subduction (Ehlig, 1981; Jacobson, 1983a, 1983b, 1997; Jacobson et al., 1996) and no model has yet been proposed to account for its exhumation.

Normal faulting alone is unlikely to have brought the Pelona schist from ~37 km depth to the surface. The detachment fault in a metamorphic core complex setting is a large-scale extensional structure that exhumes rocks from the mid-crust level. For example, the Miocene detachment fault of the Whipple Mountains in southeastern California initiated at depth of ~20 km (Behr and Platt, 2011). However, detachment faults of this type commonly sole into the localized-distributed transition zone at a depth of ~20 km (Platt et al., 2015) and are unlikely to root into a depth of ~ 37 km in a continental setting. Erosion is not plausible for exhuming the Pelona schist, either. The deep-water San Francisquito Formation in southern California was deposited from latest Cretaceous through middle Paleocene time (Kooser, 1982), indicating that the Sierra Pelona area was in a marine environment during the subduction and first stage exhumation of the Pelona schist, and erosion was likely to be minimal. The channelized extrusion model (Chapman et al., 2010) can bring up the entire subduction assemblage as a whole. We think this is unlikely to be the case for the Pelona schist, for two reasons. First, when S2 of the Pelona schist, which is defined by the retrograde metamorphic mineral assemblages, was formed between 60 Ma and 58 Ma, Pacific Ocean lithosphere was still subducting at a rate of 115 mm yr^{-1} (Doubrovine and Tarduno, 2008) using a recent plate reconstruction (Müller et al., 2008), so that schist exhumation was coeval with on-going subduction. Return flow allows the subducted material to be exhumed along roughly the same route as it descended, and makes the subduction channel a "two-way street" (Ernst, 1984). The second observation favoring return flow is that the whole of the exposed Pelona Schist in the East Fork shows evidence for large non-coaxial strains, which is not consistent with the channelized extrusion model.

In the classic return flow model, the velocity of rocks in a subduction channel results from a combination of the Couette flow driven by the drag of the subducting plate and the Poiseuille flow caused by the buoyancy of the low-density rocks in the subduction channel (Beaumont et al., 2009). In this model, the maximum subducting velocity occurs at the base of the channel, the maximum exhumation velocity occurs in the upper part of the channel, and the velocity at the roof of the channel is zero. When crossing the locus of the maximum exhumation velocity plane, the sense of shear changes because the velocity gradient changes its sign.

That is what we observed in D2. S2 shows a top-to-NW sense of shear at structurally deeper levels and a top-to-SE sense of shear at structurally shallower levels. In the return flow model the sense of shear changes from the bottom of the channel to the top, with the rocks in the return flow moving relatively northwestward. The locus of maximum exhumation velocity probably occurs around Iron Fork where we observe conflicting senses of shear. In addition, the locus of the maximum

5 exhumation velocity may have shifted through time, which would explain the conflicting shear senses in the quartz veins, metacherts, and greenschist in the Iron Fork area.

Return flow brought the Pelona schist to a depth of ~22 km, marking the first-stage of exhumation. It was immediately followed by the second-stage exhumation (Fig. 11). The mylonitized Pelona schist right beneath the Vincent fault indicates

10 that the Vincent fault exhumed the Pelona schist to 9 km depth as constrained by the thermobarometric analysis of the upper plate (Xia and Platt, in preparation). Similar extensional faulting of the upper plate has played an important role during the exhumation of other Laramide subduction-related schists from middle and lower crust to the upper crust (e.g., Chapman et al., 2010; Jacobson et al., 2002; Oyarzabal et al., 1997).

7 Rheological interpretation

15 Metagreywacke is the dominant rock-type in the Pelona schist, which takes up around 90% of the East Fork transect (Jacobson, 1983b). Albite does not develop any crystal-plastic deformation microstructures while sheet silicates were mainly deformed during S3, so quartz is likely to account for most of the strain in metagreywacke. Metachert interlayers in metagreywacke do not show boudinage or buckle folds without the surrounding metagreywacke or greenschist being involved, implying that metachert and metagreywacke were coupled during deformation. This suggests that the values of

20 strain rate measured from one type of rock can be applied to another.

7.1 D1

The absence of CPO (Fig 4c), presence of differentiated cleavage (Fig 4a), and lack of evidence of crystalline plastic deformation indicate that pressure solution was the dominant deformation mechanism during S1. Piezometry was not applicable due to the lack of dynamic recrystallization, but the shear stress estimated from S2 shows that it was likely to be

25 less than 10 MPa around the end of subduction. The peak temperature, which we presume was the temperature around the end of subduction, was 518.9 °C.

7.2 D2

7.2.1 Quartz in metagreywacke

In the metagreywacke from the lower limb of the Narrows synform, the strong differentiation of mica and other sheet silicate

30 minerals into P domains, concentration of quartz in Q domains and pressure shadows, the precipitation of quartz in the pull-

aparts of albite grains, and the existence of fluid inclusions in quartz grains indicate that pressure solution was the dominant deformation mechanism (Fig. 5 a-e). The source of the quartz is likely to have been what are now the mica-rich P-domains, and the sinks include the pressure shadows around the albite porphyroblasts. Dynamic recrystallization and undulose extinction in quartz imply that dislocation creep probably occurred immediately after if not contemporaneously with pressure

5   solution, and also contributed to the D2 deformation (Fig. 5d and f). The average recrystallized quartz grain size is ~75 μm, indicating the shear stress during recrystallization was less than 10 MPa (Table 1). It should be noted that the stress estimates here may only represent the maximum stress during pressure solution if quartz recrystallized after pressure solution during exhumation. The peak temperature is constrained to ~518.9 °C, but retrogression during D2 suggests that temperature decreased during deformation.

10   **7.2.2 Quartz in metachert**

In the lower limb of the Narrows synform, strong crystallographic preferred orientation of quartz in metachert indicates that dislocation creep was the dominant deformation mechanism in this rock-type, though in some samples the related microstructures were strongly modified by subsequent annealing, as quartz shows equant grain shapes, straight grain boundaries and 120° triple points (Fig 6a). Shear stresses calculated from recrystallized quartz or quartz grains preserved in

15   albite porphyroblasts vary between 8.6 and 13.3 MPa (Table 1).

7.3 D3

Crenulation cleavage in the hinge of the Narrows synform indicates that microfolding of the S2 foliation accompanied by pressure solution was the dominant deformation mechanism there (Fig. 8a).

20   In the upper limb of the Narrows synform, quartz in the metagreywacke underwent dynamic recrystallization. Subgrain rotation was the dominant recrystallization mechanism but bulging occurred subsequently. This suggests that quartz was mainly deformed by climb-accommodated dislocation creep. We estimate the temperature of recrystallization at approximately 390 °C. The average grainsize of recrystallized quartz grains is 18 ± 6 μm, indicating a shear stress of ~22 MPa (Table 1).

25   **8 Estimates of shear zone widths and strain rates**

S2 schistosity is well developed in the Pelona schist throughout the 4km thick transect in the eastern San Gabriel Mountains and shows thoroughly intense deformation. In order to produce a shear zone without a discernible variation in the amount of strain over a structural thickness of 4 km, we assumed the width of the subduction channel to be 10 ± 5 km. This estimation agrees well with the thickness of the observed low-velocity anisotropic layer in the middle to lower crust of the southern

30   California (Lee et al., 2014; Li et al., 1992; Porter et al., 2011). We assume that the 4km thick Pelona schist in the eastern

14

San Gabriel Mountains formed part of the zone of return flow during D2, and the remaining 6 ± 5 km-thickness of Pelona schist formed the zone of subduction flow in the channel.

5 The subduction of the protolith of the Pelona schist started no earlier than 68 Ma (Grove et al., 2003) and it reached the maximum depth by 60 Ma as discussed in Sect. 5, during which the estimated rate of convergence between Pacific Ocean lithosphere and North America was over 110 mm yr^{-1} (Doubrovine and Tarduno, 2008). This displacement rate corresponds to a strain rate of 5.8×10^{-13} s^{-1}, assuming that the deformation caused by subduction was accommodated by the 6 km-thick down-going section of the subduction channel.

10 During the first stage of exhumation, the Pelona schist was decompressed from ~10.5 kbar to ~5.8 kbar, which is approximately equivalent to a vertical exhumation of 15.1 km from 60 Ma to 58 Ma. With a channel geometry discussed in Appendix A, the displacement rate in the zone of return flow was 17 to 70 mm yr^{-1} and hence the maximum strain rate was 1.4×10^{-13} to 5.5×10^{-13} s^{-1}. The wide ranges of the displacement rate and the strain rate are primarily due to the overlapping hornblende and muscovite Ar/Ar ages.

15 The width of the mylonitized Pelona schist is ~100 m, and the lower 200-m of the mylonite zone in the hanging wall of the Vincent fault shows similar quartz microstructures and metamorphic conditions as those in the Pelona schist. Thermobarometric and geochronologic data (Xia and Platt, in preparation) from the hanging-wall mylonites show that the mylonites were decompressed to 2.4 kbar and cooled to 230°C by 43 Ma. Assuming a linear cooling history from 390°C to 20 230°C between 55 Ma and 43 Ma, the mylonites crossed the 300°C isotherm at around 48 Ma, when ductile deformation ceased. Assuming the shear zone originally dipped ~30°, the estimated average strain-rate during mylonitization was ~3.4 $\times 10^{-13}$ s^{-1}. This is slightly higher than the range of 2.6-9.3×10^{-14} s^{-1} given by the quartz dislocation creep flow law (Hirth et al., 2001) for the measured shear stress of 22 MPa (differential stress of 38 MPa).

9 Discussion

25 ### 9.1 Topography- and density-driven return flow model of subduction channels

To compare the measured values of stress and strain rate of the return flow with the geodynamic model, we used the analytical formulation given by Beaumont et al. (2009). This one-dimensional formulation assumes that the rocks in the channel have a linear viscous rheology (appropriate for pressure solution creep). The stress and strain rate profiles across the subduction channel can be calculated for a given channel geometry, viscosity of material in the channel, and the pressure 30 gradient in the subduction channel. Behr and Platt (2013) modified this formulation, so as to relate the viscosity to the maximum exhumation rate.

The buoyancy contrast between the subducting material and the overlying upper plate has been proposed as the driving force for return flow (e.g., England and Holland, 1979; Ernst et al., 1997). The density of the Pelona schist, which consists of 90% metagreywacke, is presumably ~2700 kg m^{-3}. The overriding plate, after the removal of its high-density batholithic root during the Laramide subduction, is mainly made up with felsic batholiths and felsic plutons with gabbronorite to

5   gabbrodiorite intrusives at the bottom of the crustal column (Saleeby et al., 2003). The average density of the overriding plate is assumed as 2850 kg m^{-3} with large uncertainties. Thus, the density contrast between the schist and the upper plate could be as little as 150 kg m^{-3} and might not be sufficient to initiate return flow.

The topographic gradient between the trench and the arc could act as the major driving force for return flow, as described in

10   Appendix B. The pressure gradient due to the topographic difference can be up to 969 Pa m^{-1}, whereas that caused by the density contrast is only 316 Pa m^{-1}. If D2 lasted 2 m.y., the Poiseuille flow driven by the topographic gradient can be up to 62 mm yr^{-1}, whereas that driven by the density contrast is no more than 21 mm yr^{-1} (Fig. 12).

We have modified the pressure gradient by adding the effect of topography to that generated by the density contrast, as

15   shown in Appendices B and C. With a pressure gradient caused by both topography and density contrast, the one-dimensional model given by Beaumont et al. (2009) yields a shear stress along the upper surface of the channel of ~10 MPa, and a strain-rate of 4.1×10^{-13} s^{-1} to 1.16×10^{-12} s^{-1}. These results generally agree with our estimates for the first stage exhumation of the Pelona schist.

9.2 Implications for the pressure solution flow law of quartz

20   Pressure solution is a common deformation mechanism in low-grade metamorphic conditions, but it remains poorly understood and its flow law is loosely constrained. The three primary models for pressure solution are the thin-film model (Rutter and Elliott, 1976; Weyl, 1959), the island channel model (Cox and Paterson, 1991; Raj, 1982), and the stress-corrosion micro-cracking model (den Brok, 1998; Gratz, 1991). The thin-film model assumes that the transport of dissolved material occurs by diffusion in a fluid film a few nanometers thick along grain-boundaries, and that the rate of pressure

25   solution is governed by the grain-boundary diffusivity (Rutter and Elliott, 1976; Weyl, 1959). In the island channel model the fluid fills channels that surround islands where the grain boundaries are in contact. The rate of deformation in this model is controlled by the diffusivity of solute in the fluid-filled channel (Raj, 1982). A more sophisticated model, the stress corrosion micro-cracking model, assumes that continuously produced micro-cracks along grain boundaries due to stress corrosion can cause a rough grain-surface topography, and material is transported through the plumbing network consisting

30   of grain boundary film, capillary network of the micro-cracks along grain boundaries and wide pores between grains (Gratz, 1991). In this model the rate of deformation is inversely proportional to the square of the island diameter instead of the square of the average grain diameter (also see Appendix D).

The above three models can be tested by our estimated values of the rheological parameters from the Pelona schist. Deformation of metagreywacke during D2 was dominated by pressure solution. Our strain-rate estimate for this stage is 1.4×10^{-13} to 5.5×10^{-13} s^{-1} and the shear stress was less than ~10 MPa. The grainsize of quartz in metagreywacke varies between 30 μm and 100 μm. Comparison between the above estimates and the stress-strain rate curves predicted by those

5 three models for pressure solution shows that strain-rate estimates from the Pelona schist lie between the predictions of the stress-corrosion micro-cracking model and the thin-film model, whereas that forecast by the island channel model is many orders of magnitude faster (Fig. 13).

Our strain-rate estimates are likely to be somewhat higher than those predicted by theoretical models for pressure solution in

10 pure quartz, as shown in Fig. 14a. This may be because of the abundance of white mica in Pelona schist. It has long been observed that phyllosilicates can increase rates of dissolution (Bukovská et al., 2015; Heald, 1956; Rutter and Elliott, 1976; Wassmann and Stöckhert, 2013; Weyl, 1959), and differences in electrochemical potential between unlike minerals, e.g., quartz and mica, have been proposed as the driving force of dissolution (Greene et al., 2009; Kristiansen et al., 2011; Meyer et al., 2006). Probably due to the relatively high content of white mica, metagreywacke in Pelona schist yielded a higher

15 strain-rate than the prediction of the thin-film model. This also explains the distinct deformation behavior of metachert from metagreywacke in Pelona schist. The lack of mica in metachert resulted in too low a strain-rate contribution from pressure solution, and therefore dislocation creep became the dominant deformation mechanism.

An additional factor is that dislocation creep is likely to have contributed to the bulk strain-rate estimates. Quartz shows

20 undulose extinction and dynamic recrystallization in metagreywacke samples that also reveal clear evidence of pressure solution such as differentiated cleavage and precipitation of quartz in pressure shadows. Coexistence of those two types microstructures may indicate that the total deformation resulted from both pressure solution and dislocation creep.

9.3 Transition from pressure solution to dislocation creep

When the Pelona schist entered the D3 regime, the dominant deformation mechanism of metagreywacke changed from

25 pressure solution of quartz to dislocation creep of quartz (Fig. 14b). Two differences between D2 and D3 are shear stress and temperature. Shear stresses recorded by the Pelona schist during D2 are less than those in D3, while the temperature was higher. When dynamic recrystallization is not dominant, so that the average grainsize is not controlled by stress, the strain rate caused by quartz pressure solution is proportional to the first power of differential stress (den Brok, 1998), whereas the strain rate produced by quartz dislocation creep is proportional to the fourth power of the differential stress (Hirth et al.,

30 2001). That is, quartz pressure solution is much less sensitive to stress compared to quartz dislocation creep. During S3, shear stresses increased to a few tens of megapascals and dramatically expedited dislocation creep. Thus, crystal plastic deformation became the leading deformation mechanism during S3.

Increased stress also changed the scale of the shear zone. Grainsize reduction due to dynamic recrystallization caused strain localization during S3. One clue is that the exposed width of the zone with S3 is ~100 m while S2 penetrated the entire 4km transect along the East Fork in the San Gabriel Mountains.

10 Conclusions

5   New microstructural observations, thermobarometric analysis and geochronologic data were used to constrain the deformation history and rheological properties of the Pelona schist during Late Cretaceous-Paleocene Laramide subduction. The primary conclusions are:

1) The Pelona schist preserves a record of deformational and metamorphic processes from subduction to exhumation. The Pelona schist was subducted no earlier than 68 Ma, and reached the peak P-T condition of 10.5 ± 0.4 kbar and 518.9 ± 19.6 °C by ~60 Ma, after which it underwent two stages of exhumation: first by return flow within the channel and then along the Vincent fault. By ~43 Ma the Pelona schist entered the brittle regime.

2) The dominant deformation mechanism of the Pelona schist during subduction (D1) and the first stage of exhumation (D2) was pressure solution. The presence of mica expedited quartz dissolution and may have increased the strain-rate relative to the predictions of the currently available quartz pressure-solution flow laws based on monomineralic samples.

3) During the second stage of exhumation (D3), the Pelona schist was deformed dominantly by dislocation creep. Strain localization occurred due to grainsize reduction caused by dynamic recrystallization.

4) Our estimate of shear stress during subduction and first-stage exhumation is less than 10 MPa while that during second-stage exhumation increased to 22 MPa.

5) The estimated magnitude of shear stress and strain rate in the subduction channel agrees well with the flow-channel model for linear viscous creep. Our measured stresses and strain rates during the second stage of exhumation are close to the quartz dislocation creep flow law of Hirth et al. (2001).

Acknowledgements

Appendices

A: Dip of the Laramide subduction channel

We made the following assumptions about the dip of the subduction channel when the Pelona schist was subducted:

5   1) The migration of the trench was negligible from Late Cretaceous when the magmatic arc was active to the time when the Pelona schist was subducted. This allows us to estimate the trench-arc distance;

2) Following the previous assumption, we assume that the Mesozoic trench-arc distance was approximately 250 km by comparison with the modern trench-arc gap of the northwestern United States and that the magmatic arc was about 100 km
10   wide based on the present-day outcrop of the Sierra Nevada;

3) The depth of the trench was ~4.5 km when the Pelona schist was subducted. The Laramide shallow subduction was inferred to be result of the subduction of the Hess and Shatsky conjugate oceanic plateaux (Liu et al., 2010), while the former, which originated from the mid-ocean ridge 110 to 100 m.y. before present (Vallier et al., 1983) and intersected the North
15   American plate about 70 m.y. before present (Liu et al., 2010), is spatially and temporally related to the formation of the Pelona schist. Therefore, the Pacific Ocean lithosphere adjacent to the western edge of North America was ~40 m.y. old when the Hess plateau was subducted. The bottom of a typical sea floor aged 40 m.y. is ~4.5 km beneath the sea level as constrained by present-day observations and predicted by theoretical models (Johnson and Carlson, 1992; Turcotte and Schubert, 2002). The above depth is likely to increase by another ~3 km along the trench due to buckling and flexture,
20   resulting a sea floor depth of ~7.5 km. The Hess Rise in the central North Pacific Ocean is currently about 3 km above the surrounding sea floor (Vallier et al., 1983), and if this holds true for the Hess conjugate, the overall trench depth would be ~4.5 km;

4) The depth of the subduction channel was 30 km underneath the western margin of the Mesozoic arc. This allows the
25   Pelona schist to remain beneath the Mesozoic magmatic arc after the first-stage exhumation, which is constrained by the fact that the Pelona schist and other Laramide subduction-related schists crop out within the Mesozoic arc at present day. This assumption gives a subduction channel dip of ~3.3° between the trench and the arc;

5) The depth of the subduction channel was more than 45 km at the east margin of the Mesozoic arc. This fits the
30   hypothesized ~45-60 km thick crust of the Nevadaplano which lasted well into Paleogene time (Ernst, 2009; Wernicke et al., 1996) and requires a minimum dip of 12.4° for the subduction channel underneath the arc.

Solid Earth

Discussions

Open Access

EGU

B: Topography-induced pressure gradient

Assume a monotonically increasing topography at constant rate over a transect width of l (Fig. B1). The amount of increased elevation over the interested width l is h. The slope of this transect is ω. Therefore, one has

$$h = l \cdot \tan \omega. \tag{B1}$$

5

A subduction zone dipping against the topographic slope lies underneath the slope. The dip of the subduction zone is γ. The distance between a point at the bottom of the overiding plate and the left end of the subduction zone is x. The relationship among l, x and γ is

$$l = x \cdot \cos \gamma. \tag{B2}$$

10

Combine Eq. (B1) and Eq. (B2) and one has

$$h = x \cdot \cos \gamma \cdot \tan \omega. \tag{B4}$$

The pressure P caused by the topography of the upper plate is $\rho g h$ where ρ is the density of the upper plate and g is the

15 gravitational acceleration. P can be written as

$$P = \rho g h = \rho g x \cdot \cos \gamma \cdot \tan \omega. \tag{B5}$$

P increases with x and works as the driving force of the exhumation of the rocks within the channel. The gradient of P along the subduction channel is

20 $$\frac{\partial P}{\partial x} = \rho g \cdot \cos \gamma \cdot \tan \omega = \frac{\rho g h}{l} \cdot \cos \gamma. \tag{B6}$$

The paleotopography of southern California in Late Cretaceous-Paleocene could not be readily reconstructed because of the deformation associated with the San Andreas Fault and other Cenozoic faults. However, the paleo-geomorphology of the southern end of the Great Valley and Sierra Nevada can shed light on the possible contemporaneous topography of southern

25 California.

The Late Cretaceous depositional environment in the western foothills of the southern Sierra Nevada was fluvial-deltaic (Cherven, 1983). The elevation of the western foothills of the arc is unlikely to have been higher than 0.5 km. To the east of the Mesozoic magmatic arc was the "Nevadaplano", a high and broad plain lasting from Late Cretaceous to Eocene

30 (DeCelles, 2004). Its estimated average elevation was more than 3 km (DeCelles, 2004). The Sierra Nevada magmatic arc itself, which formed the west flank of the Nevadaplano (Henry, 2009), could have had an elevation up to 4 km at approximately 70 Ma (House et al., 1998, 2001). Along the west slope of Sierra Nevada at that time, the elevation may have changed from 1 km in the west to more than 4 km in the east within a horizontal distance of ~ 80 km (House et al., 2001).

The above geometric setting and an assumed rock density of 2700 kg m^{-3} yield a pressure gradient of 969 Pa m^{-1}. In contrast, the density difference between the upper plate and the schist, which is assumed as 150 kg m^{-3}, would generate a pressure gradient of 316 Pa m^{-1} with the same geometric setting.

5 **C: Calculations of channel flow stresses and strain rates**

In a parallel-sided subduction channel with a width of L, the velocity profile in a linear viscous fluid is

$$v(z) = -\frac{\nabla P(zL - z^2)}{2\eta} + V\left(1 - \frac{z}{L}\right), \tag{C1}$$

where z is the distance to the base of the channel, ∇P the pressure gradient, η the viscosity of material in the channel, and V the subducting velocity (Beaumont et al., 2009; Behr and Platt, 2013).

10

The pressure gradient is caused by (1) the density contrast between the rocks in the subduction channel and those in the overriding plate and (2) the topography gradient as illustrated in Appendix B. The pressure gradient caused by density contrast is:

$$\nabla P_{\text{density}} = (\rho_{\text{lc}} - \rho_{\text{sc}})g \sin\gamma, \tag{C2}$$

15 where ρ_{lc} is the density of lower crust, ρ_{sc} the density of rocks in the subduction channel, g the gravity acceleration (Beaumont et al., 2009; Behr and Platt, 2013). The sum of Eq. (C2) and Eq. (B6) is the total pressure gradient:

$$\nabla P = (\rho_{\text{lc}} - \rho_{\text{sc}})g \sin\gamma + \frac{\rho g h}{l} \cdot \cos\gamma, \tag{C3}$$

The viscosity η is the lesser of the roots of Eq. (C4):

20 $$\frac{4V^2}{L^2 \nabla P}\eta^2 - 4(V - 2v_e)\eta + L^2 \nabla P = 0, \tag{C4}$$

where v_e is the maximum exhumation rate (Behr and Platt, 2013). v_e can be approximated as the ratio of d_2, displacement during D2 to t, the duration of D2.

The strain rate profile is

25 $$v'(z) = -\frac{\nabla P(L - 2z)}{2\eta} - \frac{V}{L}. \tag{C5}$$

The stress profile (Behr and Platt, 2013) is

$$\sigma(z) = v'(z) \cdot \eta = -\frac{\nabla P(L - 2z)}{2} - \frac{V\eta}{L}. \tag{C6}$$

30 Parameters used for the stress and strain rate calculations in the subduction channel are listed in Table C1.

D: Parameters used for flow law calculations

As summarized by den Brok (1998) and Behr and Platt (2013), quartz pressure solution flow laws can be written as

$$\dot{\varepsilon} = \frac{AV_{\mathrm{m}}cD_{\mathrm{gb}}w\sigma\rho_{\mathrm{f}}}{RTd^3\rho_{\mathrm{s}}},$$
(D1)

5 $$\dot{\varepsilon} = \frac{AV_{\mathrm{m}}cD_{\mathrm{fluid}}d_{\mathrm{chan}}\sigma\rho_{\mathrm{f}}}{RTd^3\rho_{\mathrm{s}}}, \text{ and}$$
(D2)

$$\dot{\varepsilon} = \frac{AV_{\mathrm{m}}cD_{gb}w\sigma\rho_{\mathrm{f}}}{RTd_{\mathrm{isl}}^2 d\rho_{\mathrm{s}}}$$
(D3)

for the thin film model, the island channel model, and the micro-cracking model, respectively, where σ is differential stress in Pa and T the absolute temperature. The descriptions and values used for the parameters in Eqs. (D1) to (D3) are listed in Table D1.

10

Quartz dislocation creep flow law (Hirth et al., 2001) is

$$\dot{\varepsilon} = Af_{\mathrm{H_2O}}\sigma^4\exp\left(-\frac{Q}{RT}\right),$$
(D4)

where A is a material parameter, $f_{\mathrm{H_2O}}$ water fugacity, σ differential stress in MPa, Q the activation energy, R the ideal gas constant, and T the absolute temperature. As constrained by Hirth et al. (2001), A equals to $10^{-11.2\pm0.6}$ MPa^{-4} s^{-1} and Q has a

15 value of 135±15 kJ mol^{-1}. Maximum water fugacity was assumed at given pressure and temperature and was computed from the fugacity calculator (https://www.esci.umn.edu/people/researchers/withe012/fugacity.htm; Pitzer and Sterner, 1994).

References

Barth, A. P. and Schneiderman, J. S.: A comparison of structures in the Andean orogen of northern Chile and exhumed midcrustal structures in southern California, USA: An analogy in tectonic style?, International Geology Review, 38(12),

20 1075–1085, doi:10.1080/00206819709465383, 1996.

Beaumont, C., Jamieson, R. A., Butler, J. P. and Warren, C. J.: Crustal structure: A key constraint on the mechanism of ultra-high-pressure rock exhumation, Earth and Planetary Science Letters, 287(1–2), 116–129, doi:10.1016/j.epsl.2009.08.001, 2009.

Behr, W. M. and Platt, J. P.: A naturally constrained stress profile through the middle crust in an extensional terrane, Earth

25 and Planetary Science Letters, 303(3–4), 181–192, doi:10.1016/j.epsl.2010.11.044, 2011.

Behr, W. M. and Platt, J. P.: Rheological evolution of a Mediterranean subduction complex, Journal of Structural Geology, 54, 136–155, doi:10.1016/j.jsg.2013.07.012, 2013.

Behr, W. M., Thomas, J. B. and Hervig, R. L.: Calibrating Ti concentrations in quartz for SIMS determinations using NIST silicate glasses and application to the TitaniQ geothermobarometer, American Mineralogist, 96(7), 1100–1106,

30 doi:10.2138/am.2011.3702, 2011.

Solid Earth
Discussions

Open Access

EGU

Berman, R. G.: Internally-consistent thermodynamic data for minerals in the system $Na_2O-K_2O-CaO-MgO-FeO-Fe_2O_3-Al_2O_3-SiO_2-TiO_2-H_2O-CO_2$, Journal of Petrology, 29(2), 445–522, doi:10.1093/petrology/29.2.445, 1988.

Beyssac, O., Goffé, B., Chopin, C. and Rouzaud, J. N.: Raman spectra of carbonaceous material in metasediments: a new geothermometer, Journal of Metamorphic Geology, 20(9), 859–871, doi:10.1046/j.1525-1314.2002.00408.x, 2002.

5 Brandon, M. T., Roden-Tice, M. K. and Garver, J. I.: Late Cenozoic exhumation of the Cascadia accretionary wedge in the Olympic Mountains, northwest Washington State, Geological Society of America Bulletin, 110(8), 985–1009, doi:10.1130/0016-7606(1998)110<0985:LCEOTC>2.3.CO;2, 1998.

den Brok, S. W. J. (Bas): Effect of microcracking on pressure-solution strain rate: The Gratz grain-boundary model, Geology, 26(10), 915–918, doi:10.1130/0091-7613(1998)026<0915:EOMOPS>2.3.CO;2, 1998.

10 Brun, J.-P. and Faccenna, C.: Exhumation of high-pressure rocks driven by slab rollback, Earth and Planetary Science Letters, 272(1–2), 1–7, doi:10.1016/j.epsl.2008.02.038, 2008.

Bukovská, Z., Wirth, R. and Morales, L. F. G.: Pressure solution in rocks: focused ion beam/transmission electron microscopy study on orthogneiss from South Armorican Shear Zone, France, Contributions to Mineralogy and Petrology, 170(3), 31, doi:10.1007/s00410-015-1186-8, 2015.

15 Burchfiel, B. C. and Davis, G. A.: Mojave Desert and environs, in The geotectonic development of California, edited by W. G. Ernst, pp. 217–252, Prentice Hall, Englewood Cliffs, New Jersey., 1981.

Chapman, A. D., Kidder, S., Saleeby, J. B. and Ducea, M. N.: Role of extrusion of the Rand and Sierra de Salinas schists in Late Cretaceous extension and rotation of the southern Sierra Nevada and vicinity, Tectonics, 29(5), 1–21, doi:10.1029/2009TC002597, 2010.

20 Cherven, V. B.: A delta-slope-submarine fan model for Maestrichtian part of Great Valley Sequence, Sacramento and San Joaquin basins, California, AAPG Bulletin, 67(5), 772–816, doi:10.1306/03B5B6AA-16D1-11D7-8645000102C1865D, 1983.

Cloos, M. and Shreve, R. L.: Subduction-channel model of prism accretion, melange formation, sediment subduction, and subduction erosion at convergent plate margins: 1. Background and description, Pure and Applied Geophysics PAGEOPH, 25 128(3–4), 455–500, doi:10.1007/BF00874548, 1988.

Coney, P. J. and Reynolds, S. J.: Cordilleran Benioff Zones, Nature, 270, 403–406, doi:10.1038/275464a0, 1977.

Cox, S. F. and Paterson, M. S.: Experimental dissolution-precipitation creep in quartz aggregates at high temperatures, Geophysical Research Letters, 18(8), 1401–1404, doi:10.1029/91GL01802, 1991.

Crowell, J. C.: An outline of the tectonic history of southeastern California, in The geotectonic development of California, 30 edited by W. G. Ernst, pp. 583–600, Prentice Hall, Englewood Cliffs, New Jersey., 1981.

DeCelles, P. G.: Late Jurassic to Eocene evolution of the Cordilleran thrust belt and foreland basin system, western U.S.A, American Journal of Science, 304(2), 105–168, doi:10.2475/ajs.304.2.105, 2004.

Dibblee, T. W. J.: Areal geology of the western Mojave Desert California, U. S. Geological Survey Professional Paper, 522, 1–153, 1967.

Dibblee, T. W. J.: Geologic map of the Crystal Lake quadrangle, Dibblee Geological Foundation Map, DF-87, 2002a.

Dibblee, T. W. J.: Geologic map of the Glendora quadrangle, Dibblee Geological Foundation Map, DF-89, 2002b.

Dibblee, T. W. J.: Geologic map of the Mount Baldy quadrangle, Dibblee Geological Foundation Map, DF-90, 2002c.

Dibblee, T. W. J.: Geologic Map of the Mount San Antonio quadrangle, Gibblee Geological Foundation Map, DF-88, 2002d.

5   Dickinson, W. R. and Snyder, W. S.: Plate tectonics of the Laramide orogeny, in Geological Society of America Memoir, vol. 151, pp. 355–366., 1978.

Doubrovine, P. V. and Tarduno, J. A.: A revised kinematic model for the relative motion between Pacific oceanic plates and North America since the Late Cretaceous, Journal of Geophysical Research, 113(B12), B12101, doi:10.1029/2008JB005585, 2008.

10 Ehlig, P. L.: Origin and tectonic history of the basement terrane of the San Gabriel Mountains, Central Transverse Ranges, in The geotectonic development of California, edited by W. G. Ernst, pp. 253–283, Prentice Hall, Englewood Cliffs, New Jersey., 1981.

England, P. C. and Holland, T. J. B.: Archimedes and the Tauern eclogites: the role of buoyancy in the preservation of exotic eclogite blocks, Earth and Planetary Science Letters, 44(2), 287–294, doi:10.1016/0012-821X(79)90177-8, 1979.

15 Ernst, W. G.: Californian blueschists, subduction, and the significance of tectonostratigraphic terranes., Geology, 12(7), 436–440, doi:10.1130/0091-7613(1984)12<436:CBSATS>2.0.CO;2, 1984.

Ernst, W. G.: Rise and fall of the Nevadaplano, International Geology Review, 51(October 2012), 583–588, doi:10.1080/00206810903063315, 2009.

Ernst, W. G., Maruyama, S. and Wallis, S.: Buoyancy-driven, rapid exhumation of ultrahigh-pressure metamorphosed
20 continental crust., Proceedings of the National Academy of Sciences of the United States of America, 94(18), 9532–9537, doi:10.1073/pnas.94.18.9532, 1997.

Farver, J. and Yund, R.: Silicon diffusion in a natural quartz aggregate: Constraints on solution-transfer diffusion creep, Tectonophysics, 325(3–4), 193–205, doi:10.1016/S0040-1951(00)00121-9, 2000.

Fournier, R. O. and Potter, R. W.: An equation correlating the solubility of quartz in water from 25° to 900°C at pressures up
25 to 10,000 bars, Geochimica et Cosmochimica Acta, 46(10), 1969–1973, doi:10.1016/0016-7037(82)90135-1, 1982.

Gerya, T. V. and Stockhert, B.: Exhumation rates of high pressure metamorphic rocks in subduction channels: The effect of Rheology, Geophysical Research Letters, 29(8), 1261, doi:10.1029/2001GL014307, 2002.

Graham, C. M. and England, P. C.: Thermal regimes and regional metamorphism in the vicinity of overthrust faults: an example of shear heating and inverted metamorphic zonation from southern California, Earth and Planetary Science Letters,
30 31(1), 142–152, doi:10.1016/0012-821X(76)90105-9, 1976.

Graham, C. M. and Powell, R.: A garnet-hornblende geothermometer: calibration, testing, and application to the Pelona Schist, Southern California, Journal of Metamorphic Geology, 2(1), 13–31, doi:10.1111/j.1525-1314.1984.tb00282.x, 1984.

Gratz, A. J.: Solution-transfer compaction of quartzites: progress toward a rate law, Geology, 19(9), 901–904, doi:10.1130/0091-7613(1991)019<0901:STCOQP>2.3.CO, 1991.

Greene, G. W., Kristiansen, K., Meyer, E. E., Boles, J. R. and Israelachvili, J. N.: Role of electrochemical reactions in pressure solution, Geochimica et Cosmochimica Acta, 73(10), 2862–2874, doi:10.1016/j.gca.2009.02.012, 2009.

Grigull, S., Krohe, A., Moos, C., Wassmann, S. and Stöckhert, B.: "Order from chaos": A field-based estimate on bulk rheology of tectonic mélanges formed in subduction zones, Tectonophysics, 568–569, 86–101,
5   doi:10.1016/j.tecto.2011.11.004, 2012.

Grove, M., Jacobson, C. E., Barth, A. P. and Vucic, A.: Temporal and spatial trends of Late Cretaceous–early Tertiary underplating of Pelona and related schist beneath southern California and southwestern Arizona, Geological Society of America Special Paper, 374, 381–406, doi:10.1130/0-8137-2374-4.381, 2003.

Hamilton, W.: Tectonic setting and variations with depth of some Cretaceous and Cenozoic structural and magmatic systems
10   of the western United States, in Metamorphism and crustal evolution of the western United States, edited by W. G. Ernst, pp. 1–40, Prentice Hall, Englewood Cliffs, New Jersey., 1988.

Heald, M. T.: Cementation of Simpson and St. Peter Sandstones in Parts of Oklahoma, Arkansas, and Missouri, The Journal of Geology, 64(1), 16–30, doi:10.1086/626314, 1956.

Henry, C. D.: Uplift of the Sierra Nevada, California, Geology, 37(6), 575–576, doi:10.1130/focus062009.1, 2009.

15   Hirth, G., Teyssier, C. and Dunlap, J.: An evaluation of quartzite flow laws based on comparisons between experimentally and naturally deformed rocks, International Journal of Earth Sciences, 90(1), 77–87, doi:10.1007/s005310000152, 2001.

Holyoke, C. W. and Kronenberg, A. K.: Accurate differential stress measurement using the molten salt cell and solid salt assemblies in the Griggs apparatus with applications to strength, piezometers and rheology, Tectonophysics, 494(1–2), 17–31, doi:10.1016/j.tecto.2010.08.001, 2010.

20   House, M. A., Wernicke, B. P. and Farley, K. A.: Dating topography of the Sierra Nevada, California, using apatite (U–Th)/He ages, Nature, 396(November), 66–69, doi:10.1038/23926, 1998.

House, M. A., Wernicke, B. P. and Farley, K. A.: Paleo-geomorphology of the Sierra Nevada, California, from (U-Th)/He ages in apatite, American Journal of Science, 301(2), 77–102, doi:10.2475/ajs.301.2.77, 2001.

Houston, H.: Low friction and fault weakening revealed by rising sensitivity of tremor to tidal stress, Nature Geoscience,
25   8(5), 409–415, doi:10.1038/ngeo2419, 2015.

Huang, R. and Audétat, A.: The titanium-in-quartz (TitaniQ) thermobarometer: A critical examination and re-calibration, Geochimica et Cosmochimica Acta, 84, 75–89, doi:10.1016/j.gca.2012.01.009, 2012.

Jacobson, C.: Relationship of deformation and metamorphism of the Pelona Schist to movement on the Vincent thrust, San Gabriel Mountains, southern California, American Journal of Science, 283, 587–604, 1983a.

30   Jacobson, C.: Structural geology of the Pelona Schist and Vincent thrust, San Gabriel Mountains, California, Geological Society of America Bulletin, 94(June), 753–767, 1983b.

Jacobson, C.: Qualitative thermobarometry of inverted metamorphism in the Pelona and Rand Schists, southern California, using calciferous amphibole in mafic schist, Journal of Metamorphic Geology, 13, 79–92, 1995a.

Jacobson, C.: Structural and metamorphic evolution of the Orocopia Schist and related rocks, southern California: Evidence

for late movement on the Orocopia fault, Tectonics, 14(4), 933–944, 1995b.

Jacobson, C.: Metamorphic convergence of the upper and lower plates of the Vincent thrust, San Gabriel Mountains, southern California, USA, Journal of Metamorphic Geology, 15, 155–165, 1997.

Jacobson, C., Oyarzabal, F. and Haxel, G.: Subduction and exhumation of the Pelona-Orocopia-Rand schists, southern
5 California, Geology, 24(6), 547–550, 1996.

Jacobson, C. E.: Petrological evidence for the development of refolded folds during a single deformational event, Journal of Structural Geology, 6(5), 563–570, doi:10.1016/0191-8141(84)90065-8, 1984.

Jacobson, C. E.: The $^{40}Ar/^{39}Ar$ geochronology of the Pelona schist and related rocks, southern California, Journal of Geophysical Research, 95(B1), 509–528, doi:10.1029/JB095iB01p00509, 1990.

Jacobson, C. E. and Dawson, M. R.: Structural and metamorphic evolution of the Orocopia Schist and related rocks,
10 southern California: Evidence for late movement on the Orocopia fault, Tectonics, 14(4), 933–944, doi:10.1029/95TC01446, 1995.

Jacobson, C. E., Grove, M., Stamp, M. M., Vucic, A., Oyarzabal, F. R., Haxel, G. B., Tosdal, R. M. and Sherrod, D. R.: Exhumation history of the Orocopia Schist and related rocks in the Gavilan Hills Exhumation history of the Orocopia Schist
15 and related rocks in the Gavilan Hills area of southeasternmost California, Geological Society of America Special Paper, 365, 129–154, doi:10.1130/0-8137-2365-5.129, 2002.

Jacobson, C. E., Grove, M., Vućić, A., Pedrick, J. N. and Ebert, K. A.: Exhumation of the Orocopia Schist and associated rocks of southeastern California: Relative roles of erosion, synsubduction tectonic denudation, and middle Cenozoic extension, Geological Society of America Special Paper, 419, 1–37, doi:10.1130/978-0-8137-2419-5, 2007.

20 Jennings, C. W.: Geologic map of California., 1977.

Joesten, R.: Grain growth and grain-boundary diffusion in quartz from the Christmas Mountains (Texas) contact aureole, American Journal of Science, 283–A, 233–254, 1983.

Johnson, H. P. and Carlson, R. L.: Variation of sea floor depth with age: A test of models based on drilling results, Geophysical Research Letters, 19(19), 1971–1974, doi:10.1029/92GL01946, 1992.

25 Kidder, S. and Ducea, M. N.: High temperatures and inverted metamorphism in the schist of Sierra de Salinas, California, Earth and Planetary Science Letters, 241(3–4), 422–437, doi:10.1016/j.epsl.2005.11.037, 2006.

Kooser, M.: Stratigraphy and Sedimentology of the type San Francisquito Formation, southern California, Pacific Section SEPM, 22, 53–61, 1982.

Kristiansen, K., Valtiner, M., Greene, G. W., Boles, J. R. and Israelachvili, J. N.: Pressure solution - The importance of the
30 electrochemical surface potentials, Geochimica et Cosmochimica Acta, 75(22), 6882–6892, doi:10.1016/j.gca.2011.09.019, 2011.

Kruhl, J. H.: Reply: Prism- and basal-plane parallel subgrain boundaries in quartz: a microstructural geothermobaromether, Journal of Metamorphic Geology, 16, 142–146, doi:10.1046/j.1525-1314.1996.00413.x, 1998.

Law, R. D.: Deformation thermometry based on quartz c-axis fabrics and recrystallization microstructures: A review, Journal

Solid Earth
Discussions

Open Access

EGU

of Structural Geology, 66, 129–161, doi:10.1016/j.jsg.2014.05.023, 2014.

Lee, E., Chen, P., Jordan, T. H., Maechling, P. B., Denolle, M. A. M. and Beroza, G. C.: Full-3-D tomography for crustal structure in Southern California based on the scattering-integral and the adjoint-wavefield methods, Journal of Geophysical Research: Solid Earth, 119(8), 6421–6451, doi:10.1002/2014JB011346, 2014.

5   Li, Y.-G., Henyey, T. L. and Silver, L. T.: Aspects of the crustal structure of the western Mojave Desert, California, from seismic reflection and gravity data, Journal of Geophysical Research, 97(B6), 8805–8816, doi:10.1029/91JB02119, 1992.

Liu, L., Gurnis, M., Seton, M., Saleeby, J., Müller, R. D. and Jackson, J. M.: The role of oceanic plateau subduction in the Laramide orogeny, Nature Geoscience, 3(5), 353–357, doi:10.1038/ngeo829, 2010.

Massonne, H.-J. and Schreyer, W.: Phengite geobarometry based on the limiting assemblage with K-feldspar, phlogopite,
10   and quartz, Contributions to Mineralogy and Petrology, 96(2), 212–224, doi:10.1007/BF00375235, 1987.

Meyer, E. E., Greene, G. W., Alcantar, N. A., Israelachvili, J. N. and Boles, J. R.: Experimental investigation of the dissolution of quartz by a muscovite mica surface: Implications for pressure solution, Journal of Geophysical Research: Solid Earth, 111(8), 2–5, doi:10.1029/2005JB004010, 2006.

Miller, F. and Morton, D.: Comparison of granitic intrusions in the Pelona and Orocopia Schists, southern California, US
15   Geological Survey Journal of Research, 5, 643–649, 1977.

Müller, R. D., Sdrolias, M., Gaina, C. and Roest, W. R.: Age, spreading rates, and spreading asymmetry of the world's ocean crust, Geochemistry, Geophysics, Geosystems, 9(4), doi:10.1029/2007GC001743, 2008.

Oyarzabal, F. R., Jacobson, C. E. and Haxel, G. B.: Extensional reactivation of the Chocolate Mountains subduction thrust in the Gavilan Hills of southeastern California, Tectonics, 16(4), 650–661, doi:10.1029/97TC01415, 1997.

20   Paterson, M. S.: A theory for granular flow accommodated by material transfer via an intergranular fluid, Tectonophysics, 245(3–4), 135–151, doi:10.1016/0040-1951(94)00231-W, 1995.

Pitzer, K. S. and Sterner, S. M.: Equations of state valid continuously from zero to extreme pressures for H2O and CO2, The Journal of Chemical Physics, 101(4), 3111–3116, doi:10.1063/1.467624, 1994.

Platt, J. P.: Exhumation of high-pressure rocks: a review of concepts and processes, Terra Nova, 5(2), 119–133,
25   doi:10.1111/j.1365-3121.1993.tb00237.x, 1993.

Platt, J. P., Behr, W. M. and Cooper, F. J.: Metamorphic core complexes: windows into the mechanics and rheology of the crust, Journal of Geological Society, doi:10.1144/jgs2014-036, 2015.

Porter, R. and Zandt, G.: Pervasive lower-crustal seismic anisotropy in Southern California: Evidence for underplated schists and active tectonics, Lithosphere, 3(3), 201–220, doi:10.1130/L126.1, 2011.

30   Porter, R., Zandt, G. and McQuarrie, N.: Pervasive lower-crustal seismic anisotropy in Southern California: Evidence for underplated schists and active tectonics, Lithosphere, 3(3), 201–220, doi:10.1130/L126.1, 2011.

Raj, R.: Creep in polycrystalline aggregates by matter transport through a liquid phase, Journal of Geophysical Research, 87(B6), 4731–4739, doi:10.1029/JB087iB06p04731, 1982.

Ring, U., Will, T., Glodny, J., Kumerics, C., Gessner, K., Thomson, S., Güngör, T., Monié, P., Okrusch, M. and Drüppel, K.:

Early exhumation of high-pressure rocks in extrusion wedges: Cycladic blueschist unit in the eastern Aegean, Greece, and Turkey, Tectonics, 26(2), TC2001, doi:10.1029/2005TC001872, 2007.

Ruff, L. J. and Tichelaar, B. W.: What Controls the Seismogenic Plate Interface in Subduction Zones?, in Geophysical Monograph: American Geophysical Union, vol. 96, edited by G. E. Bebout, D. W. Scholl, S. H. Kirby, and J. P. Platt, pp. 105–111, American Geophysical Union, Washington, D. C., 1996.

Rutter, E. H. and Elliott, D.: The kinetics of rock deformation by pressure solution [and Discussion], Philosophical Transactions of the Royal Society A: Mathematical, Physical and Engineering Sciences, 283(1312), 203–219, doi:10.1098/rsta.1976.0079, 1976.

Saleeby, J., Ducea, M. and Clemens-Knott, D.: Production and loss of high-density batholithic root, southern Sierra Nevada, California, Tectonics, 22(6), doi:10.1029/2002TC001374, 2003.

Stipp, M. and Tullis, J.: The recrystallized grain size piezometer for quartz, Geophysical Research Letters, 30(21), 1–5, doi:10.1029/2003GL018444, 2003.

Stipp, M., Tullis, J. and Behrens, H.: Effect of water on the dislocation creep microstructure and flow stress of quartz and implications for the recrystallized grain size piezometer, Journal of Geophysical Research, 111(B4), B04201, doi:10.1029/2005JB003852, 2006.

Stipp, M., Tullis, J., Scherwath, M. and Behrmann, J. H.: A new perspective on paleopiezometry: Dynamically recrystallized grain size distributions indicate mechanism changes, Geology, 38(8), 759–762, doi:10.1130/G31162.1, 2010.

Stöckhert, B.: Stress and deformation in subduction zones: insight from the record of exhumed metamorphic rocks, Geological Society, London, Special Publications, 200(1), 255–274, doi:10.1144/GSL.SP.2001.200.01.15, 2002.

Thomas, J. B., Watson, E. B., Spear, F. S., Shemella, P. T., Nayak, S. K. and Lanzirotti, A.: TitaniQ under pressure: the effect of pressure and temperature on the solubility of Ti in quartz, Contributions to Mineralogy and Petrology, 160(5), 743–759, doi:10.1007/s00410-010-0505-3, 2010.

Thomas, J. B., Watson, E. B., Spear, F. S. and Wark, D. A.: TitaniQ recrystallized: experimental confirmation of the original Ti-in-quartz calibrations, Contributions to Mineralogy and Petrology, 169(3), 27, doi:10.1007/s00410-015-1120-0, 2015.

Turcotte, D. L. and Schubert, G.: Geodynamics, 2nd ed., Cambridge University Press, Cambridge., 2002.

Vallier, T. L., Dean, W. E., Rea, D. K. and Thiede, J.: Geologic evolution of Hess Rise, central North Pacific Ocean, Geological Society of America Bulletin, 94(11), 1289–1307, doi:10.1130/0016-7606(1983)94<1289:GEOHRC>2.0.CO;2, 1983.

Wark, D. A. and Watson, E. B.: TitaniQ: a titanium-in-quartz geothermometer, Contributions to Mineralogy and Petrology, 152(6), 743–754, doi:10.1007/s00410-006-0132-1, 2006.

Wassmann, S. and Stöckhert, B.: Rheology of the plate interface — Dissolution precipitation creep in high pressure metamorphic rocks, Tectonophysics, 608, 1–29, doi:10.1016/j.tecto.2013.09.030, 2013.

Watson, E. B. and Wark, D. a.: Diffusion of dissolved SiO2 in H2O at 1 GPa, with implications for mass transport in the crust and upper mantle, Contributions to Mineralogy and Petrology, 130(1), 66–80, doi:10.1007/s004100050350, 1997.

Wernicke, B., Clayton, R., Ducea, M., Jones, C. H., Park, S., Ruppert, S., Saleeby, J., Snow, J. K., Squires, L., Fliedner, M., Jiracek, G., Keller, R., Klemperer, S., Luetgert, J., Malin, P., Miller, K., Mooney, W., Oliver, H. and Phinney, R.: Origin of High Mountains in the Continents: The Southern Sierra Nevada, Science, 271(5246), 190–193, doi:10.1126/science.271.5246.190, 1996.

5   Weyl, P. K.: Pressure solution and the force of crystallization: a phenomenological theory, Journal of Geophysical Research, 64(11), 2001–2025, doi:10.1029/JZ064i011p02001, 1959.

Xia, H. and Platt, J. P.: Is the Vincent fault in southern California the Laramide subduction zone megathrust?, n.d.

Yin, A.: Passive-roof thrust model for the emplacement of the Pelona-Orocopia Schist in southern California, United States, Geology, 30(2), 183–186, doi:10.1130/0091-7613(2002)030<0183:PRTMFT>2.0.CO;2, 2002.

10

Table 1: Stress estimates

Domain	Location	Sample #	Rock type	Recrystallized grain size (µm)	# of grains	Piezometric stress (MPa)	Shear stress (MPa)
S3	Beneath Vincent Fault	PS35	Metagreywacke	25 ± 5	102	37.9 +7.5/-5.2	21.9 +4.3/-3.0
S2	Iron Fork	PS106	Metachert	82 ± 25	78	14.8 +5.1/-2.9	8.6 +3.0/-1.7
S2	Iron Fork	PS98	Metachert	47 ± 14	123	23.1 +7.3/-4.3	13.3 +4.2/-2.5
S2	Iron Fork	PS96	Metachert	51 ± 17	249	21.5 +8.2/-4.4	12.4 +4.8/-2.5
S2	Iron Fork	PS140	Metachert	61 ± 16	93	18.8 +5.0/-3.1	10.9 +2.9/-1.8
S2	Fish Fork	PS131	Metachert	56 ± 23	195	19.9 +10.2/-4.7	11.5 +5.9/-2.7
S2	Fish Fork	PS191	Metagreywacke	72 ± 17	95	16.5 +4.1/-2.6	9.5 +2.4/-1.5
S2	Fish Fork	PS188	Metagreywacke	77 ± 19	42	15.5 +4.0/-2.5	8.9 +2.3/-1.5
S2	Prairie Fork	PS187	Metachert	66 ± 22	92	17.5 +6.7/-3.6	10.1 +3.9/-2.1

Table C1: Parameters used for subduction channel calculations

Parameter	Description	Value	Reference and notes
L	Subduction channel width [km]	10 ± 5	Lee et al. (2014); Porter and Zandt, (2011)
V	Subduction rate [mm yr^{-1}]	115	(Doubrovine and Tarduno, 2008)
d_2	Displacement during D2 [km]	70.2	Exhumed from 37 km deep to 22 km deep along a subduction channel dipping 12.4° as estimated in Appendix A
t	Duration of D2 [Myr]	1–4	Sect. 5.4
ρ_{lc} - ρ_{sc}	Density contrast between the overriding plate and the subduction channel [kg m^{-3}]	150	The density of lower crust is assumed as 2850 kg m^{-3} and that of the Pelona schist is 2700 kg m^{-3}

5 **Table D1: Parameters used for pressure solution calculations**

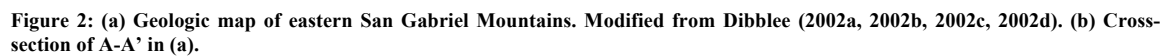| Parameter	Description	Value	Reference and notes
A	Grain shape constant	44	den Brok (1998); 44 for spheric grains
V_m	Solid molar volume [m^3 mol^{-1}]	2.269×10^{-5}	Berman (1988)
c	Solubility of solid in fluid phase	P and T dependent	Fournier and Potter (1982)
D_{gb}	Grain boundary diffusivity	T dependent	Farver and Yund (2000)
D_{fluid}	Diffusivity in grain boundary fluid	T dependent	Watson and Wark (1997)
d_{chan}	Width of island channel [µm]	0.1	den Brok (1998)
d_{isl}	Island diameter [µm]	0.5	Paterson (1995)
w	Effective width of grain boundary [nm]	100	Joesten (1983)
ρ_f	Density of fluid [g cm^{-3}]	0.923	Behr and Platt (2013)
ρ_s	Density of solid [g cm^{-3}]	2.65	Behr and Platt (2013)
R	Gas constant [J K^{-1} mol^{-1})]	8.314	
d	Grain size	Varies by sample	

Solid Earth
Discussions

Open Access

EGU
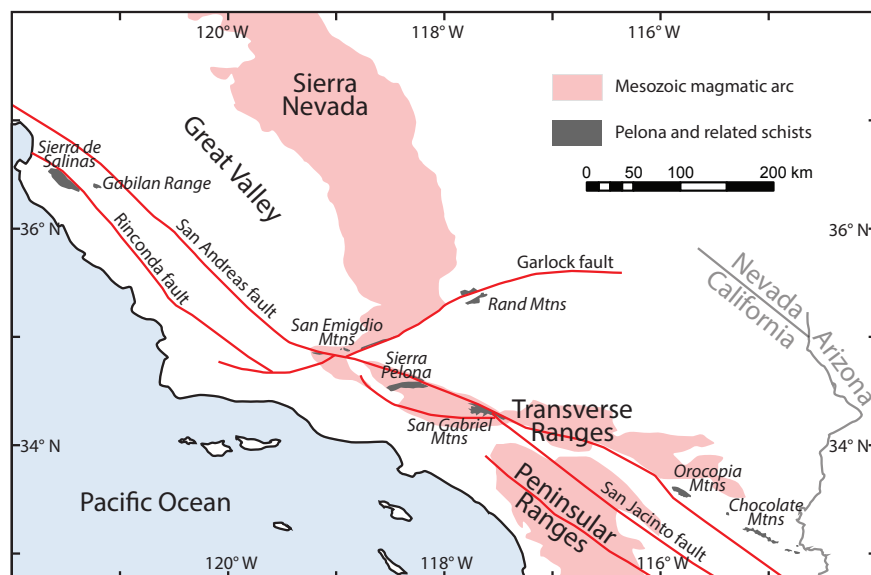
Figure 1: Regional tectonic map of southern California showing outcrops of Laramide subduction related schists, Mesozoic magmatic arc, and major faults. Modified from Jennings (1977).
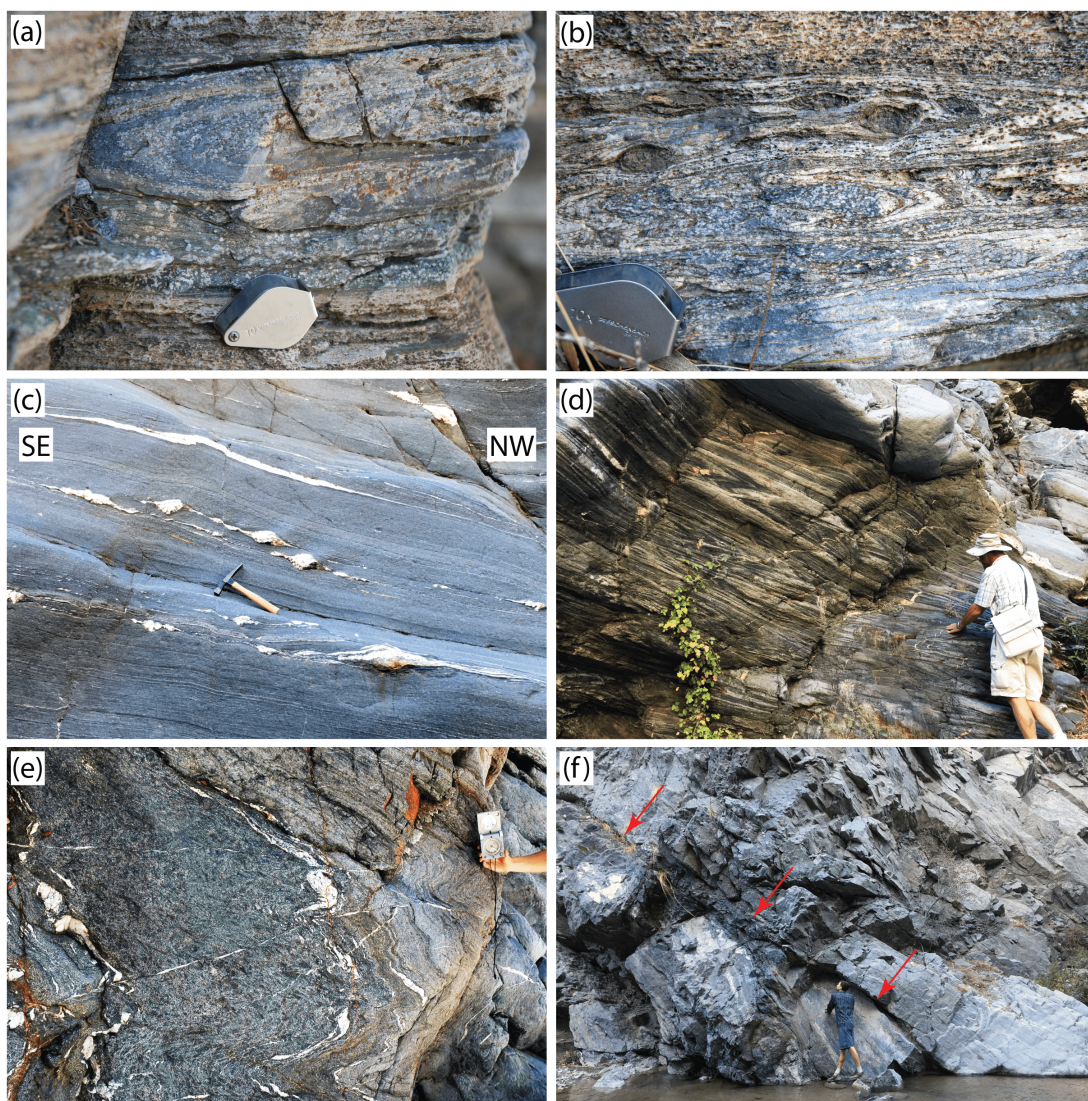
Figure 2: (a) Geologic map of eastern San Gabriel Mountains. Modified from Dibblee (2002a, 2002b, 2002c, 2002d). (b) Cross-section of A-A' in (a).

Figure 3: Outcrops of Pelona schist. Photo locations are listed in Table S1. (a) D2 folds in metachert. (b) Sheath folds in metachert. (c) Greenschist with quartz boudinage. (d) D2 folds in metagreywacke. (e) Minor D3 folds in the hinge of the Narrows synform. (f) Vincent fault as shown by the arrows. Viewing SE.

Solid Earth
Discussions

Open Access

EGU
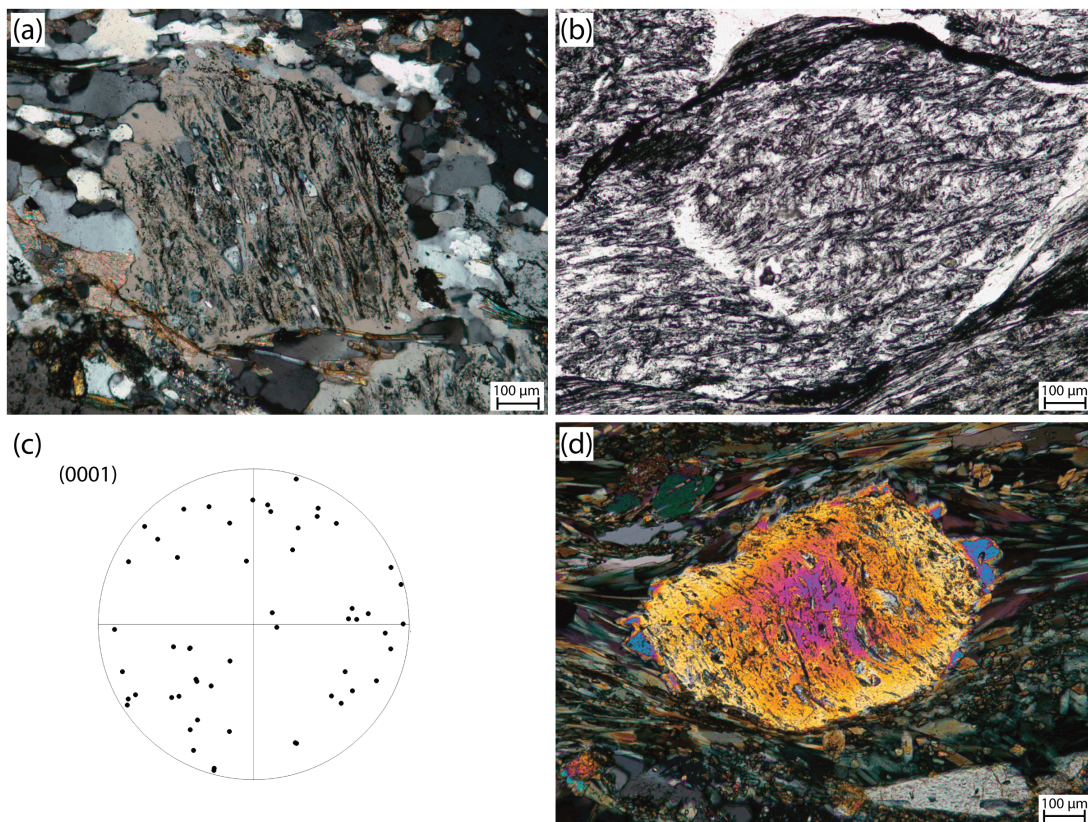
Figure 4: S1 fabric in metagreywacke and greenschist. See Table S1 for sample locations. (a) The mineral inclusions in albite outline S1. Note the differentiated cleavage. Sample PS52. (b) S1 is crenulated as shown by the trails of graphite, suggesting that more than one fabric may have formed at this time. Sample PS109. (c) CPO of quartz inclusions in one albite porphyroblast in Sample PS52. (d) S1 in greenschist shown by the mineral inclusions in the epidote porphyroblast. Sample 95.

Solid Earth
Discussions

Open Access

EGU
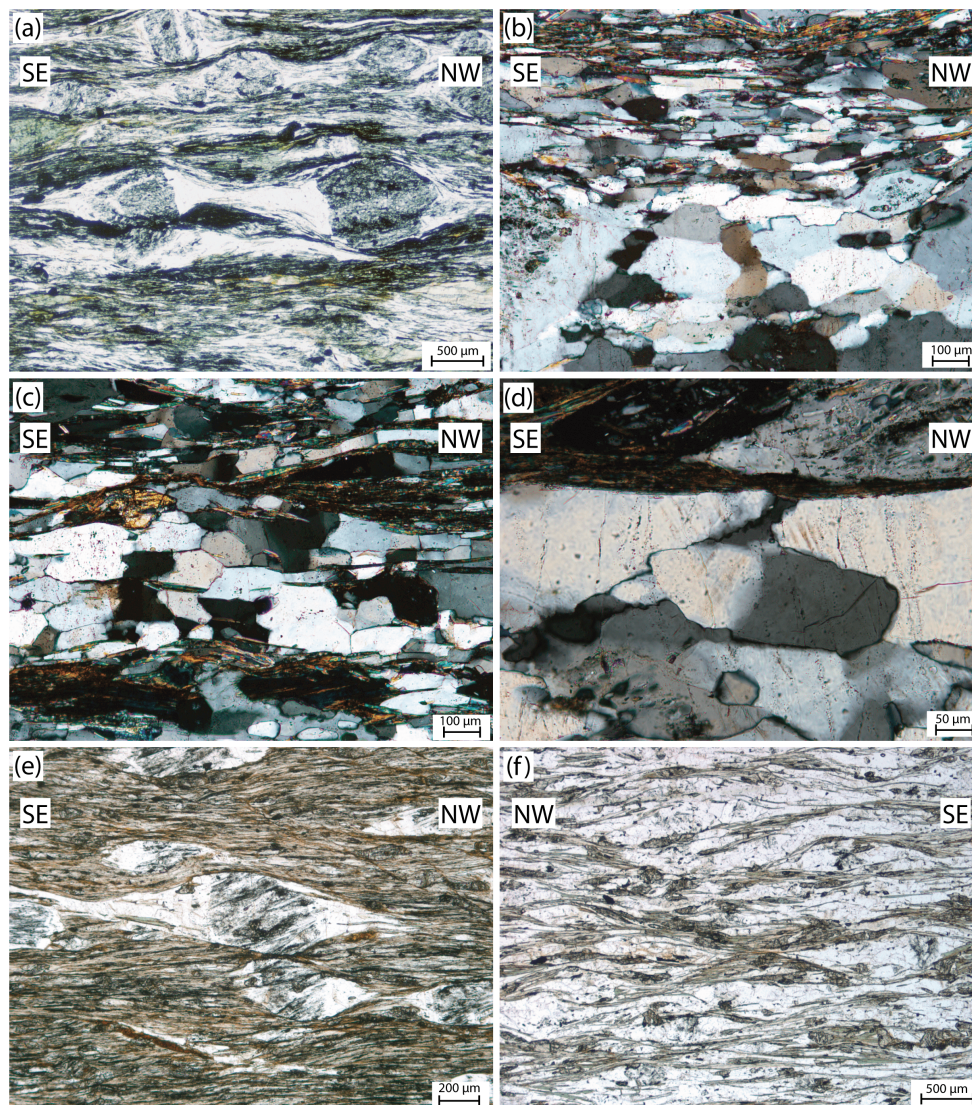
Figure 5: S2 fabric in metagreywacke. Sample locations are listed in Table S1. (a) Quartz filled between two pulled-apart ablite porphyroblasts in the center of the image. Sample PS107. (b) Quartz precipitated in the pressure-shadows between albite porphyroblasts. Sample PS185. (c) Q-domain in Sample PS190. (d) Undulose extinction and bulging in quartz grains precipitated in pressure shadows in Sample PS185 (e) Shear bands and asymmetric albite porphyroblast tails show a top-to-NW sense of shear. Sample PS185. (f) Conjugate shear bands outlined by muscovite and chlorite in Sample PS139.
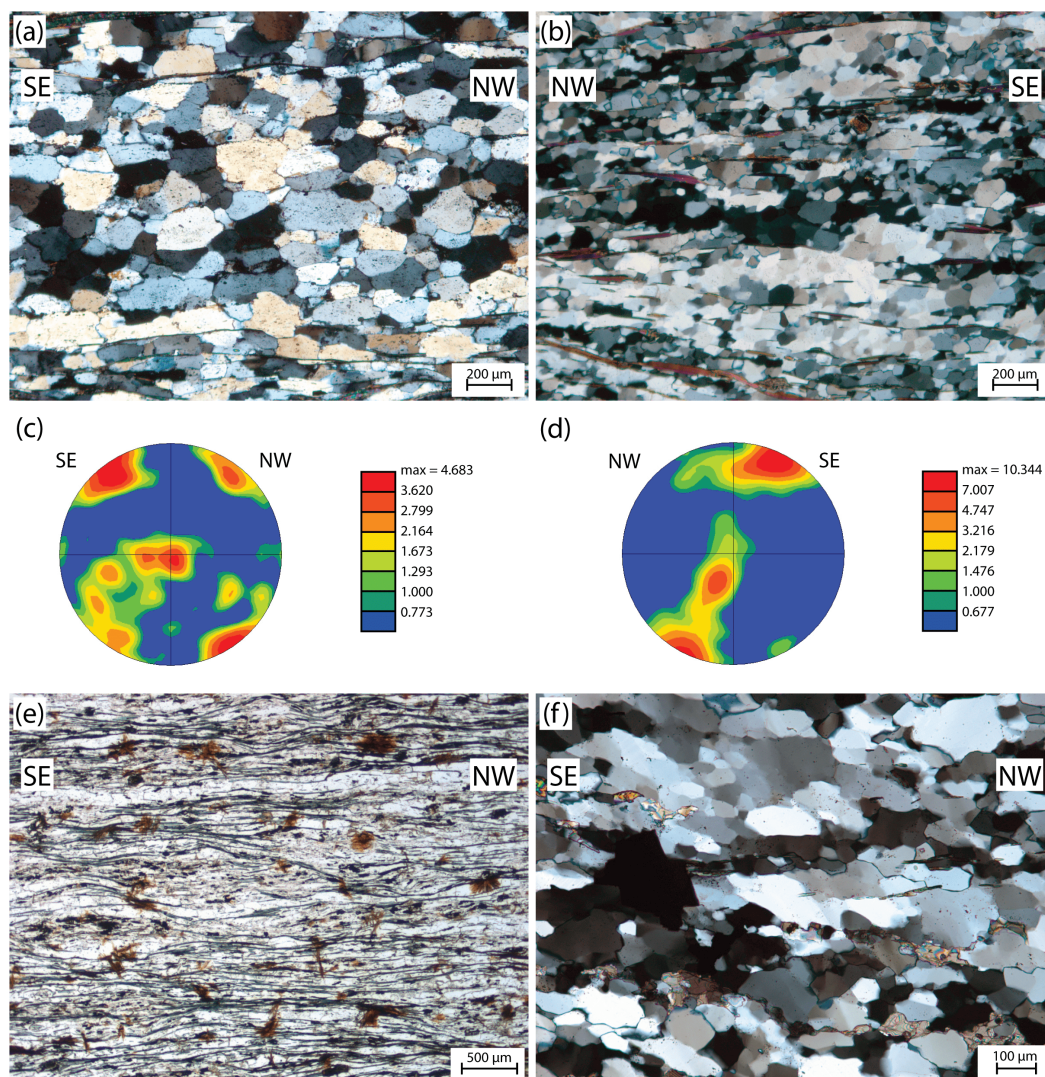
Figure 6: (a) Metachert from Prairie Fork (Sample PS186) and (c) its quartz CPO. The sense of shear cannot be inferred from (a) due to the lack of indicators. The quartz c-axis pole figure in (c) shows a vague top-to-SE sense of shear. See text for discussion. (b) Metachert from Iron Fork (Sample PS103) and (d) its quartz CPO. Both quartz new grain fabric in (b) and quartz c-axis pole figure in (c) show a top-to-SE sense of shear. Note the grainsize difference between (a) and (b). (e) Metachert with greenish needle-shaped amphibole and brown stilpnomelane. Sample PS131 from Fish Fork. Shear bands defined by amphiboles exhibit a top-to-NW sense of shear. (f) Metachert sample (PS100) from Iron Fork. The quartz new grain shape fabric and tilted prismatic subgrain walls indicate that the sense of shear was top-to-SE. Sample locations are available Table S1.
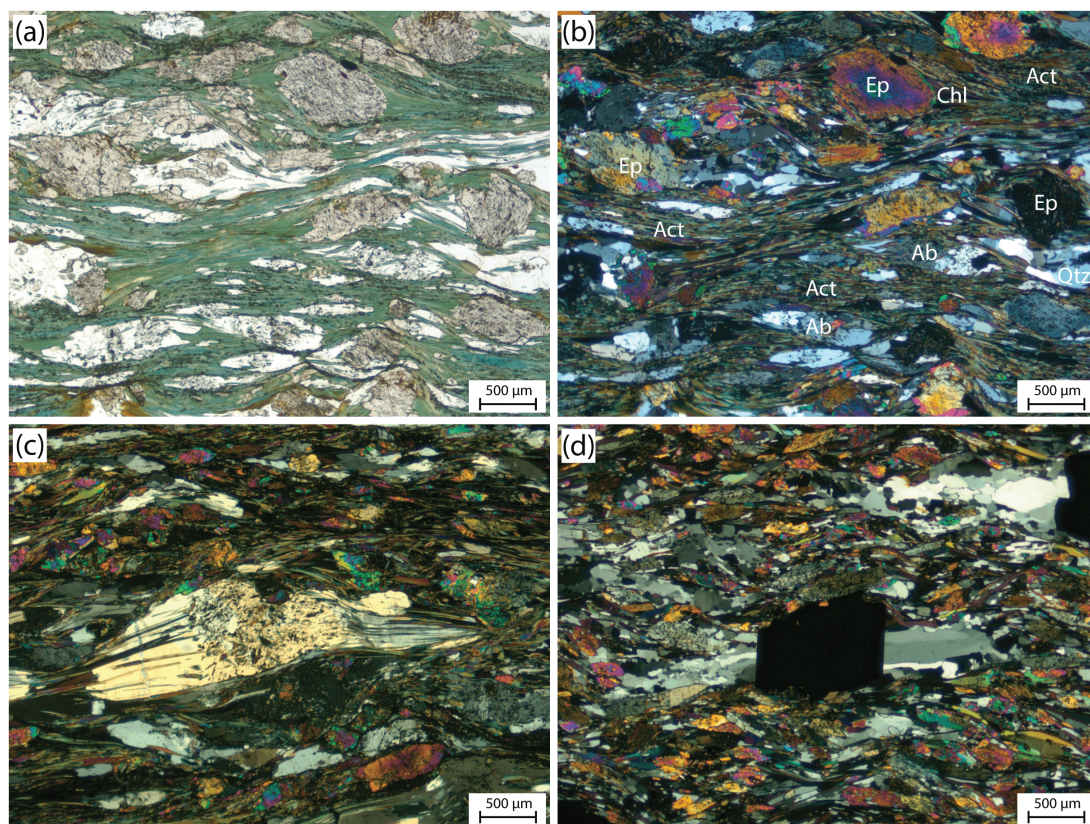
Figure 7: Mafic greenschist (sample PS95) showing S2 fabric under (a) plane light and (b) crossed polarized light. Ab: albite; Act: actinolite; Chl: Chlorite; Ep: epidote; Qtz: quartz. (c) Crystallographically continuous overgrowths on an albite porphyroblast in mafic greenschist. Sample PS97. (d) Fibrous quartz strain shadow around a magnetite crystal in mafic greenschist. Sample PS101. Locations of samples can be found in Table S1.
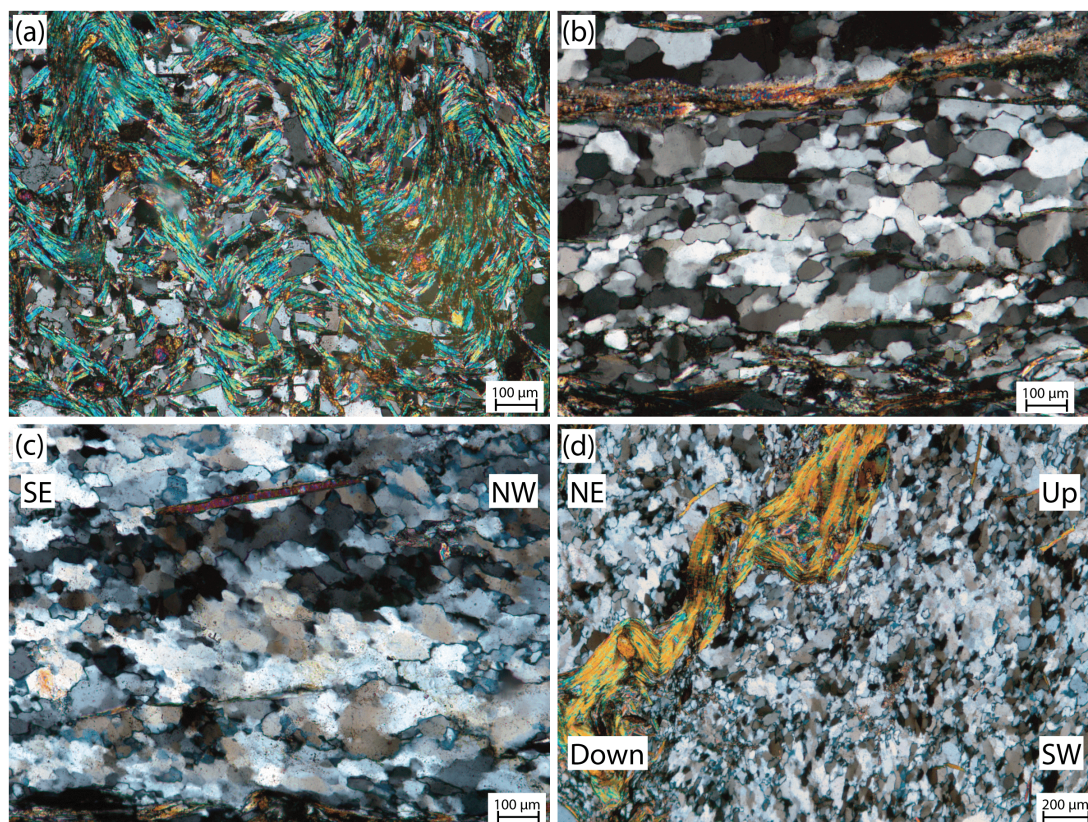
Figure 8: (a) D3 crenulations in Sample PS32 from the hinge of the Narrows synform. **(b)** Recrystallized quartz close to the hinge of the Narrows synform. Sample PS52. **(c)** Quartz in a mylonitized metagreywacke sample (PS36). **(d)** Lineation-perpendicular view of the mylonitized metagreywacke. S3 defined by the crenulated muscovite is sub-vertical, and so is the quartz shape preferred orientation. Sample PS35. See Table S1 for sample locations.
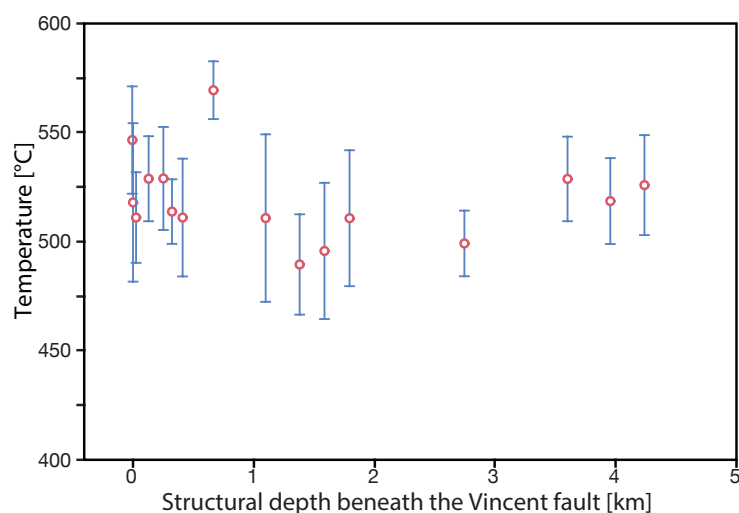
Figure 9: Peak temperature of Pelona schist constrained by laser Raman spectroscopy. See Tables S1 and S2 for sample locations and detailed results.
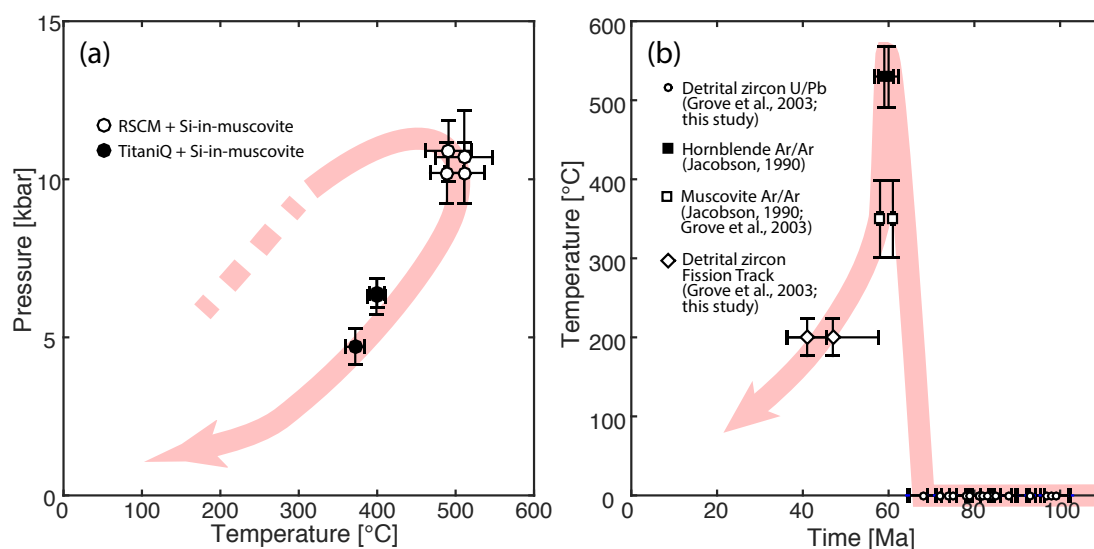
5   **Figure 10: (a) P-T-t path and (b) thermal history of Pelona schist.**
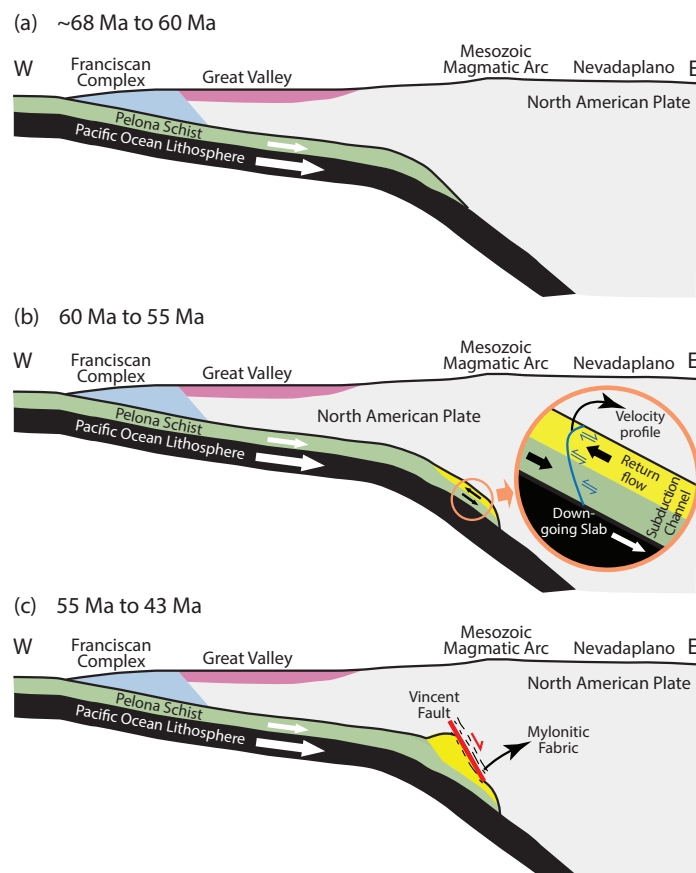
Figure 11: Tectonic model of the Pelona schist. Close-up view in (b) showing the velocity profile of the material in the subduction channel.
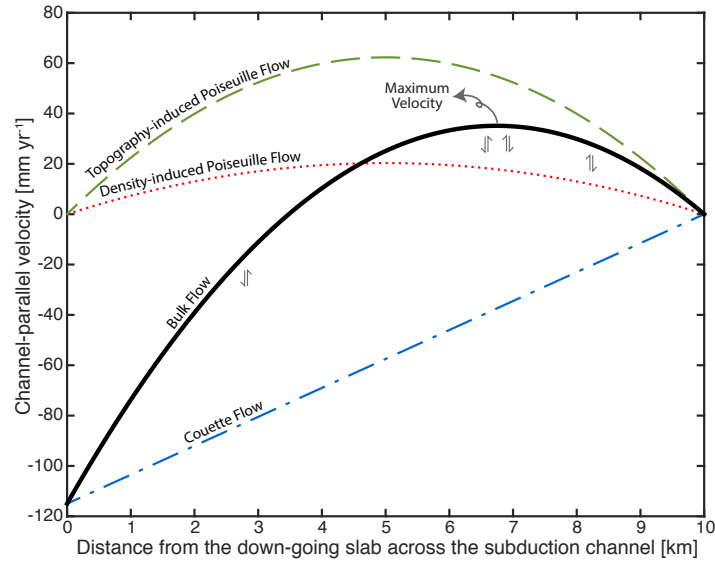
Figure 12: Velocity profile across the subduction channel filled by linear viscous material. Subduction velocity is negative and exhumation velocity is positive. Blue dash-point line: Couette flow caused by the drag of the subducting plate; red dotted curve: Poiseuille flow driven by the buoyancy of the material in the subduction channel; green dashed curve: topography induced Poiseuille flow; thick black solid curve: the bulk flow of rocks in the subduction channel. Note the sense of shear changes when crossing the maximum velocity. The duration of D2 was 2 m.y. for calculation. See Appendix C for detail.
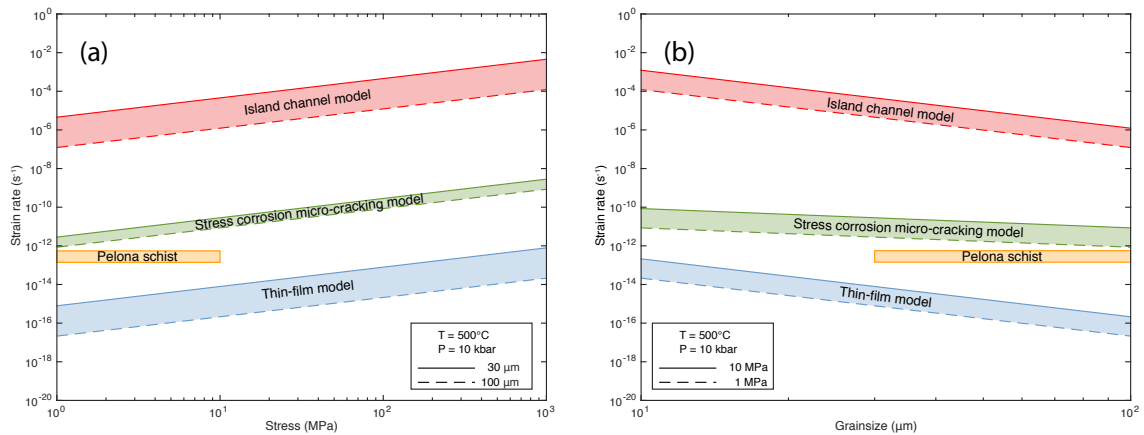
Figure 13: (a) Stress-strain-rate curve and (b) grainsize-strain-rate curve of three pressure solution flow laws. The orange zones are the estimated strain-rate of the Pelona schist.
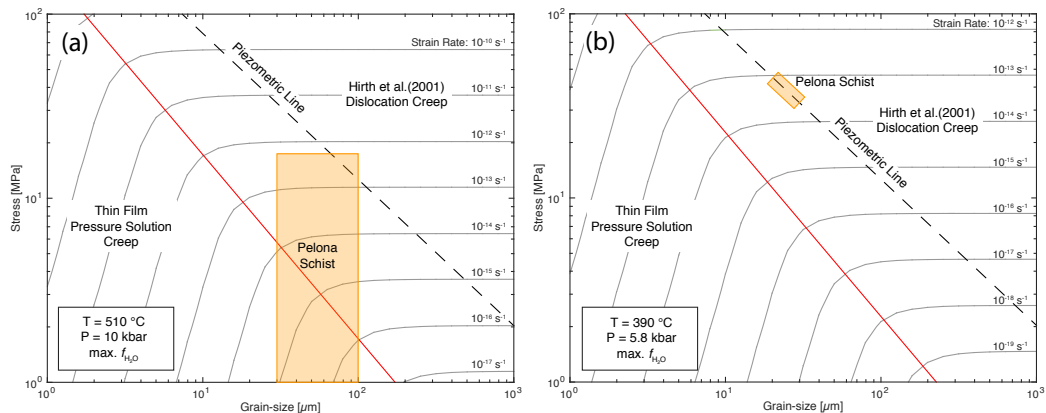
Figure 14: Deformation mechanism maps for (a) D2 and (b) D3. In both maps, the red line marks the boundary between the regime of quartz pressure solution and that of quartz dislocation creep, the black dashed line is calculated using recrystallized quartz grainsize piezometer (Stipp and Tullis, 2003), and the orange shaded area is the Pelona schist in the grainsize-stress space. See text for discussion.
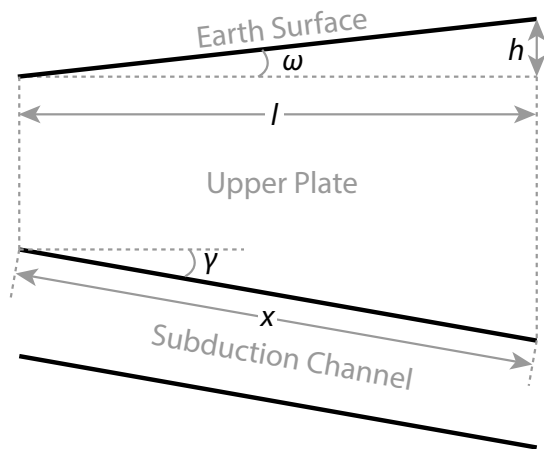
Figure B1: Geometry of topography and subduction channel.